Master's thesis

NTNU
Norwegian University of Science and Technology
Faculty of Engineering
Department of Mechanical and Industrial Engineering

Terje Tvenning

Wall thickness and scale effect on the quasi static compression and fatigue performance of AlSi10Mg sheet based lattices fabricated via selective laser melting

Master's thesis in Mechanical Engineering
Supervisor: Seyed Mohammed Javad Razavi
Co-supervisor: Zhuo Xu 'Loker'
June 2022

NTNU
Kunnskap for en bedre verden

Terje Tvenning

Wall thickness and scale effect on the quasi static compression and fatigue performance of AlSi10Mg sheet based lattices fabricated via selective laser melting

Master's thesis in Mechanical Engineering
Supervisor: Seyed Mohammed Javad Razavi
Co-supervisor: Zhuo Xu 'Loker'
June 2022

Norwegian University of Science and Technology
Faculty of Engineering
Department of Mechanical and Industrial Engineering

NTNU
Norwegian University of
Science and Technology

Master Thesis

by

Terje Tvenning

at the

Norwegian University of Science and Technology

Preface

This thesis is the result of 20 weeks of work during the spring of 2022, and concludes my M.Sc. degree at the Department of Mechanical and Industrial Engineering, at NTNU Trondheim.

The many hours spent in labs, testing, and studying, have been an exciting and rewarding for me, although challenging at times. Lattice structures, fatigue, and parametric analysis being only some of the many topics i have gained greater knowledge about throughout this project.

Also, I would like to express my gratitude to my supervisor Seyed Mohammed Javad Razavi and PhD Candidate Zhuo Xu 'Loker' for their valuable and constructive suggestions during the planning and execution of this thesis.

ABSTRACT

AM technology has opened the possibility of manufacturing lattice structure (AKA architected materials, metamaterials) that was previously not obtainable through standard manufacturing methods. In later years, these materials have seen a shift from only being produced in medical devices and interventions to increased attention in structural and otherwise industries where lightweight and high-strength materials are beneficial. Here, unlike in the biomedical field, the dimensions of the lattice are orders of magnitude larger, and the various effects are not entirely understood. Hence, there is a significant incentive to determine how the mechanical behavior of lattice structures depends on their scale and features from micrometer to centimeter.

The objective of this thesis was to determine the effects of scale, size, and wall thickness on the mechanical and fatigue properties of sheet-based gyroid lattice structures AM fabricated with AlSi10Mg. In doing so, the specimens were tested to static compression and cyclic compression to measure yield strength, Young's modulus, fatigue strength, and corresponding behavior. A parametric study of the three effects was completed by utilizing this data. In addition, CT scanning and SEM (scanning electron microscope) were employed to determine deviations in the produced geometry and examine the failure mechanisms, respectively.

Amongst several findings, the CT scanning provided a clear relationship between the cube size of a specimen and the deviation from the intended geometry, of which the smallest cube sizes deviated the most. With the SEM imagery, similar exposed locations for crack development were found, along with fracture mechanics dependent on wall thickness and the amount of load. The static compression demonstrated that yield strength increased proportionally to the volume fraction and that more porous structures were more susceptible to sequential collapses. The fatigue strength varied substantially in the parametric study of the three effects. The capacity against fatigue favored smaller scales and cube sizes for the scale and cube size effect. In terms of the wall thickness effect, the fatigue strength increased proportionally to the wall thickness, although the behavior between low and high cycle fatigue hinted at different failure mechanisms.

However, due to large deviations between the intended and actual parameters that define the three groups, it was difficult to substantiate the theoretical effects as opposed to the inaccuracies through the fabrication process on fatigue behavior. As such, some methods were proposed to ensure minor differences between nominal and actual geometry.

SAMMENDRAG

AM-teknologi har åpnet muligheten for å produsere gitterstruktur metamaterialer som tidligere ikke var tilgjengelig gjennom standard produksjonsmetoder. I senere år har disse materialene sett et skifte fra kun å bli produsert i medisinsk utstyr og intervensjoner til økt oppmerksomhet i strukturell industri og andre industrier hvor lette og høyfaste materialer er fordelaktige. Her, i motsetning til i det biomedisinske feltet, er dimensjonene til metamaterialet mye større, og de ulike effektene er ikke helt forstått. Derfor er det et betydelig insentiv til å bestemme hvordan den mekaniske oppførselen til metamaterialet avhenger av deres skala og funksjoner fra mikrometer til centimeter.

Målet med denne oppgaven var å bestemme effekten av skala, størrelse og veggtykkelse på de mekaniske egenskapene og utmattingsegenskapene til gyroide gitterstrukturer AM produsert med AlSi10Mg. Ved å gjøre dette ble prøvene testet i statisk kompresjon og syklisk kompresjons for å måle flytegrense, Youngs modul, utmattelsesstyrke og tilsvarende oppførsel. En parametrisk studie av de tre effektene ble fullført ved å bruke disse dataene. I tillegg ble CT-skanning og SEM (skanning elektronmikroskop) brukt for å bestemme avvik i den produserte geometrien og undersøke sviktmekanismene.

Blant flere funn ga CT-skanningen en klar sammenheng mellom kubestørrelsen til en prøve og avviket fra den tiltenkte geometrien, hvorav de minste kubestørrelsene hadde høyest avvik. Med SEM-bildene ble det funnet lignende eksponerte steder for sprekkutvikling, sammen med bruddmekanikk avhengig av veggtykkelse og belastningsmengde. Den statiske kompresjonen viste at flytegrensen økte proporsjonalt med volumfraksjonen og at mer porøse strukturer var mer utsatt for sekvensiell kollaps. utmattingsstyrken varierte betydelig i det parametriske studiet av de tre effektene. Kapasiteten mot utmatting favoriserte mindre skalaer og kubestørrelser, mens når det gjelder veggtykkelseseffekten, økte utmattingsstyrken proporsjonalt med veggtykkelsen, selv om oppførselen mellom lav- og høysyklus utmatting antydet forskjellige sviktmekanismer.

På grunn av store avvik mellom tiltenkte og faktiske parametere som definerer de tre gruppene, var det vanskelig å underbygge de teoretiske effektene i motsetning til unøyaktighetene gjennom fabrikasjonsprosessen på utmattelsesatferd. Av den grunn ble noen metoder foreslått for å sikre mindre forskjeller mellom nominelle og faktisk geometri.

Contents

List of Figures

List of Tables

Symbols and Abbreviations

Table 1: Symbols

Symbol	Description	Unit
$\bar{\rho}$	Relative Density	%
ρ	Density of Cellular Material	$\frac{g}{mm^3}$
ρ_0	Density of Solid Material	$\frac{g}{mm^3}$
$\frac{\Delta\varepsilon_p}{2}$	Plastic Strain Amplitude	%
ε_f'	Fatigue Ductility Coefficient	-
C	Fatigue Ductility Exponent	-
σ	Stress	MPa
σ_a	Stress Amplitude	MPa
A	Fatigue strength Coefficient	MPa
B	Fatigue Strength Exponent	-
N	Cycles	-
ρ_{Actual}	Actual Relative Density	-
$\frac{V_{Object}}{}$	Volume of Lattice Structure	mm^3
V_{Total}	Cube volume	mm^3
F	Force	N
A_{cs}	Cross-sectional Area	mm^2
K	Stiffness	$\frac{KN}{mm}$
L	Deformation Length	mm

Table 2: Abbreviations

Abbreviations	Description
AM	Additive Manufacturing
SEM	Scanning Electron Microscope
CT	Computertomografi
TPMS	Triply Perodic Minimal Surface
M	Maxwell's Number
b	Number of struts
n	Number of Nodes
CAD	Computer Aided Design
RP	Rapid Prototyping
RM	Rapid Manufacturing
PBF	Powder Bed Fusion
L-PBF	Laser Powder Bed Fusion
EB-PBF	Electron Beam Powder Bed Fusion
HCF	High Cycle Fatigue
LCF	Low Cycle Fatigue
DMLS	Direct Metal Laser Sintering
SLM	Selective Laser Melting
BCC	Body Centered Cubic
BCCZ	Body Centered Cubic Z-struts
FCC	Face Centered Cubic
VC	Vertex Cube
ECC	Edge Centre Cube
STL	Standard Tessellation Language
DIC	Digital Image Correlation

1 Introduction

1.1 Background

Nowadays, the global medical device market has experienced phenomenal growth and remarkable developments. It has been offering excellent methods for repairing or replacing missing tissues and organs in the human body, such as bones, skins, or cartilage, thanks to the lattice structures as scaffolds. On the other hand, the new lattice structures (AKA architected materials, metamaterials, etc.) are facing increasing attention in structural industries with the improvement in the field of additive manufacturing of metal, making it viable for complicated parts like these, which is nearly impossible to fabricate with conventional methods. These parts, unlike the biomedical field, are in orders of magnitude larger dimensions. Based on the preliminary results in this research group, there is a significant dependency of the mechanical behavior of lattice structures to their scale from micrometer to tens of centimeter. Therefore, it is fundamentally important to understand the mechanical properties. While some has conducted studies on the geometry of the lattice structure itself ([20], [19], [23], [14], [31], [22]), others has analysed various heat and annealing treatment for lattice structures fabricated with various types of material ([17], [11], [7], [12]). Another important aspect that has been widely considered is how lattice structures behave with regards to fatigue ([15], [24], [18], [36]), how manufacturing parameters influence the mechanical properties ([17], [16]) and some has simply looked at how relative density and size differences influence the mechanical performance of the lattice structure ([32], [34], [35], [33], [21]). On the other hand, studies that examine the scale, size, and wall thickness effect compared to fatigue behavior have not been explored to the same extent. Knowing these effects of metamaterials can be highly appreciated in industries requiring highly specialized and lightweight materials that can operate under cyclic loading.

1.2 Problem Description

Although AM technology has seen a surge of attention and becoming more common as a manufacturing tool in many industries, there are still numerous downsides to this fabrication technique, especially in the case of lattice structures. To mention a few, the surface roughness, internal porosity, and dimensional accuracy compared to the conventional methods are poor, which negatively impacts mechanical properties. In the case of fatigue strength, this is even more problematic as these defects already introduce cracks to the system, forming stress concentrations that speed up the process, ultimately resulting in premature failure. Moreover, many industries that want to utilize these AM fabricated metamaterials are working with large dimension parts. With such a high dependency on the mechanical behavior of lattice structures with varying scale, size, and wall thickness, it is a field that requires more research.

1.3 Project Scope

This research aims to study the effect of scale, size, and wall thickness on the mechanical and fatigue properties of sheet-based gyroid lattice structures AM fabricated with AlSi10Mg. The other parameters stay constant to determine the significance of these three groups systematically. More specifically, constant porosity for the scale effect, constant wall thickness for the cube size effect, and constant cube size for the wall thickness effect. The groups will be tested under both cyclic compression-compression loading to obtain fatigue data in addition to static compression testing. The specimens will then be further analyzed using SEM (Scanning Electron Microscope) to view the fatigue failure locations more closely and the surface roughness and overhangs regions. CT scanning will also be utilized to determine variations between the lattice structure's real and modeled geometry.

1.3.1 Objectives

- Compare real and model geometry with CT scan data.
- Perform static test.
- Perform fatigue tests on the lattice specimens under cyclic loading at various stresses.
- Analyse fracture mechanics, locations, surface roughness and overhang regions with SEM.

1.3.2 Research Questions

- How do the different sets compare between modeled and actual geometry?
- How do scale, cube size, and wall thickness affect fatigue life and mechanical behavior?
- How do the failure mechanics vary between the sets?

1.4 Thesis Structure

1. Introduce the technology and the problem description of this thesis.
2. Overview of relevant theory in the field of lattice structures, AM and fatigue.
3. Overview of relevant research of AM and lattice structures.
4. Overview of the material and methodology process.
5. In-depth analysis and discussion of the experimental results.
6. Conclusion and suggested further research.

2 Theory and Literature Review

Two recent and complex literature reviews on "mechanical properties towards fatigue-tolerant design and fabrication of architected cellular materials" [3] and "Properties and applications of additively manufactured metallic cellular materials" [9], was published. The former discusses the "progress to date in the improvement of the fatigue performance of cellular structures manufactured by additive manufacturing (AM)," whereas the latter focuses on "the unique properties of AM lattice structures and how these have been successfully employed for specific applications so far." Given the comprehensive nature of the two reviews within the field of fatigue and AM of lattice structures, they are the primary sources of material in this section, not to mention the articles referenced in both reviews.

2.1 Basics, Terminology and Mechanical Properties of Cellular Structures

According to these papers, "Architected meta-materials" or "cellular materials" is a new class of engineered materials characterized by their multifunctional properties, which mainly derives from the architected geometry that allows for extreme lightweight design as well as high local tolerability by varying local density. "cellular materials" refer to the fact that a regular arrangement of struts and nodes or other periodic geometries are repeated in 3D space. These unit cells can be divided into three categories, namely strut-based (A), skeletal (B), and sheet-based (C) Triply periodic minimal surface (TPMS), as seen in Figure 1. The latter two are TPMS created mathematically to obtain a zero-mean curvature at all given points. In addition, these type of unit cells has no self-intersecting or enfolded surfaces allowing for a continuing geometry that eliminates any thickness variations. As such, TPMS lattices are often reported to have smaller stress concentrations than their counterpart, the strut-based lattices. With attention to the difference between the skeletal and sheet-based TPMS, the skeletal lattice structure is designed such that the volume separated by the TPMS is filled to create a solid structure, whereas the sheet TPMS is simply thickened to create the solid structure. Either way, both TMPS methodologies facilitate a smooth geometry, absent of any nodes and points. In any case, these cellular structures excel in industries such as the biomedical, aerospace, and automotive industries as a direct outcome of the self-tailored mechanical properties achieved through modulating the unit cell in terms of geometry, scale, and relative density. The prospects are wast as a cellular structure can range far in the material properties space in terms of stiffness, strength, energy absorption, permeability, thermal conductivity, and various other properties, hence the name "meta-materials" [3, 9].

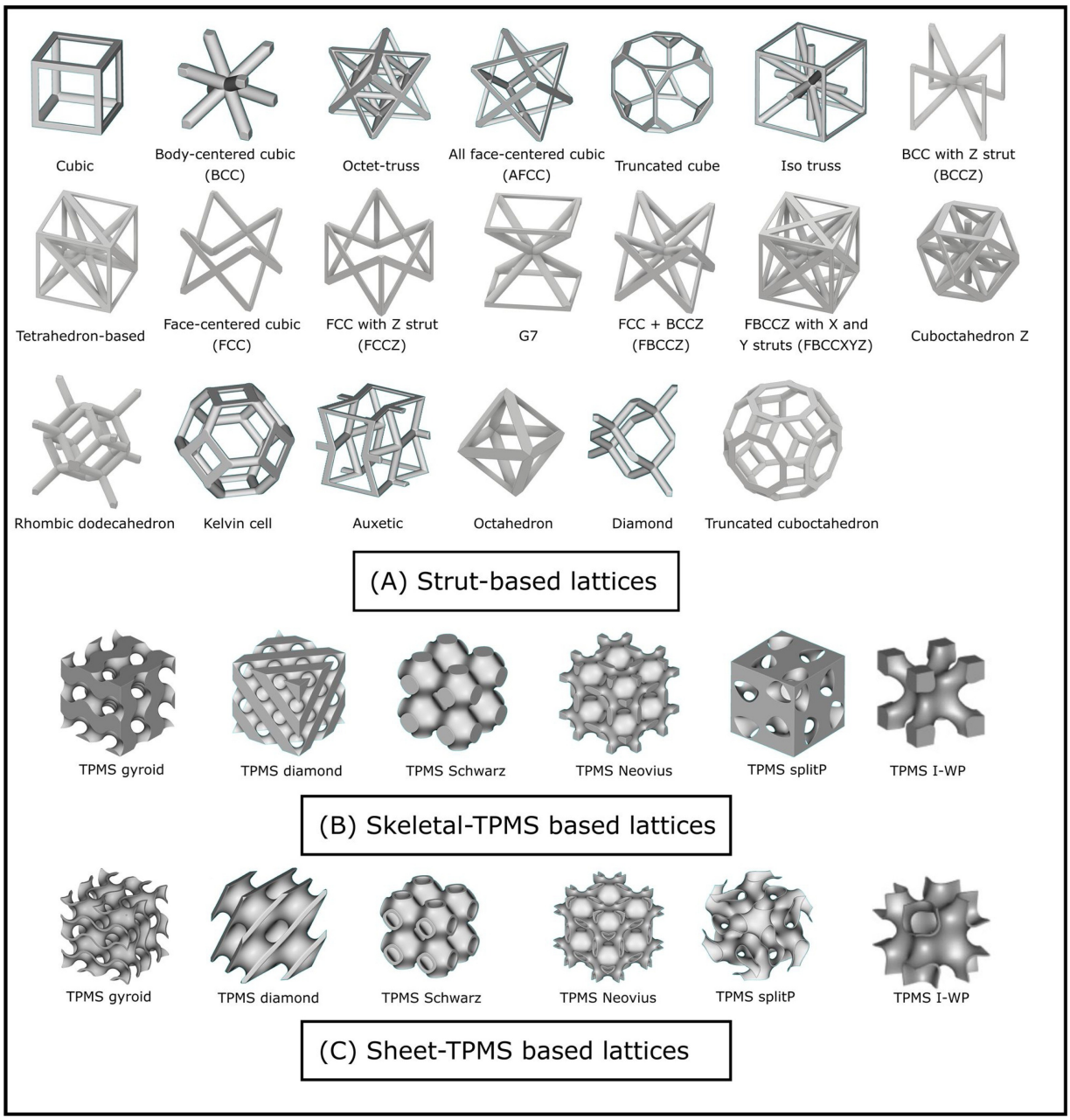

Figure 1: Various types of lattice structures [3]

There are some useful concepts with cellular structures that help describe and identify certain behaviors. The first to be discussed is a classification criterion that distinguishes between bending- and stretching-dominated structures by analyzing the nodal connectivity. To demonstrate, frame (a) and (b) in Figure 2 represent a bending- and stretch- dominated structures, respectively. When frame (a) is loaded, and the nodal connections are assumed to be fixed in space, the applied load induces bending moments on the struts, whereas in the case of the latter frame (b), the frame is evidently going to collapse due to axial stretching of the central strut, even though some of the other struts are under bending loads. Correspondingly, strut-based lattices can also be determined by either bending or stretch dominated in view of how failure presents itself. With the intention of identifying the rigidity of a structure, the Maxwell stability criterion is often used (as

presented in Equation 1), which takes the number of struts (b) and nodes (j) into account, and returns the coefficient M, also termed Maxwell's number. With a positive M, the structure can be described as stretch-dominated. On the other hand, a negative M means that the structure is bending-dominated. Deshpande et al. continue to explain that in terms of strength, stretching-dominated structures, in the realms of foams, are expected to be approximately ten times as stiff and three times as strong as bending-dominated structures [6]. This and other apparent differences between the two can be recognized when comparing their stress-strain curves illustrated in Figure 3. To begin the three phases outlining the curves. The first is the linear elastic regime (1) that last up to yielding, followed by the plateau regime (2), and lastly, the densification phase (3), where neighboring cells come into contact with one another. During phase one, it is once more illustrated the higher yield and stiffness a stretched-dominated cellular structure provides compared to its counterpart. By phase two, the difference between the two instances amounts to the compression failure mechanisms after initial yielding. A stretch-dominated lattices experience progressive failure, referring to the repeated crushing of layers, which depicts a post-yield softening accommodated by peak stress afterward, as portrayed in the figure. In contrast, a bending-dominated structure experience a steady progression and transferring of stresses due to the compliant nature of the geometry [2]. As different applications have distinct requirements for the mechanical behavior of the lattice structure, knowing the Maxwell number can therefore be advantageous and insightful to better anticipate its features as M.F Ashby explained: "if stiffness and strength at low weight are sought, the lattice must be configured in such a way that bending is prevented, leaving strut-stretching as the dominant mode of deformation" [2].

Another useful concept for porous materials such as these is the relative density which specifies the material fraction upon which the strength of a given meta-material is often represented. The explanation behind this is simply put that adding material to an already existing geometry is bound to increase the overall cross-section, consequently yielding a higher strength. From equation 2, the relative density ($\bar{\rho}$) is defined as the ratio of the density of the cellular material (ρ) to the density of the solid material (ρ_0). Although the relative density is integral to the total strength of a cellular structure, the definition of strength for porous structures also relies heavily on other factors such as geometry and scale, not to mention the many process parameters considered during fabrication. For instance, two lattices with the same relative density, one being stretch-dominated and the other being bending-dominated, will have a completely different outcome regarding the mechanical properties and failure mechanism. The same can be said for identical lattices that utilize different process parameters during fabrication.

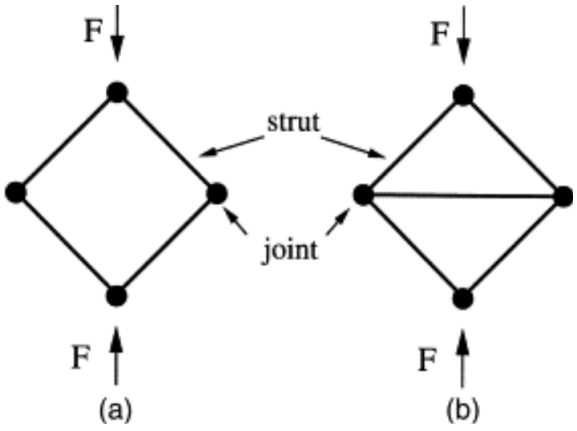

Figure 2: Bending- (a) and stretch- (b) dominated structure [6]

$$M = b - 3j + 6 \tag{1}$$

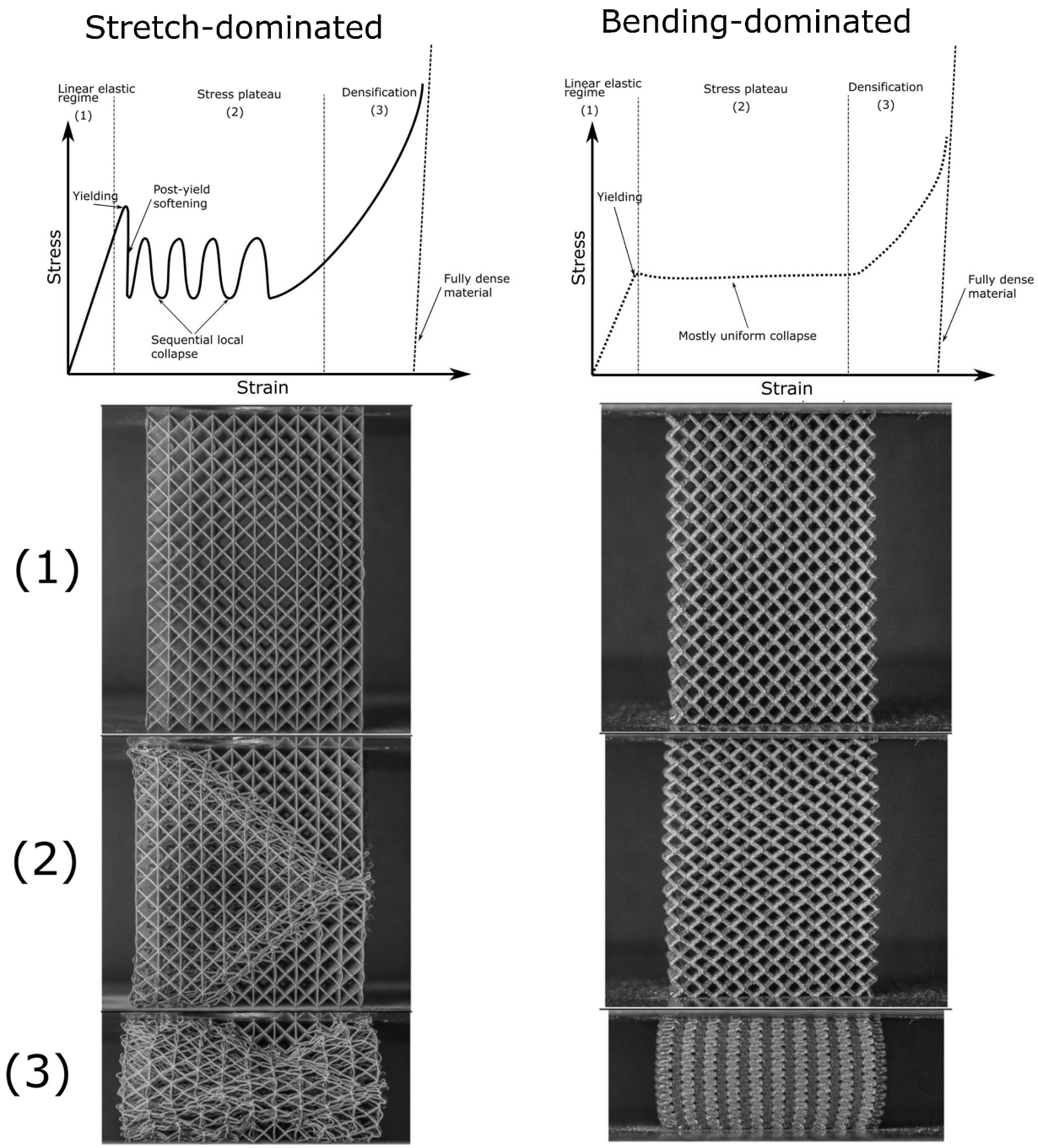

Figure 3: Compressive stress-strain curves for stretched and bending dominated cellular structures [3]

$$\bar{\rho} = \frac{\rho}{\rho_0} \tag{2}$$

2.2 Additive Manufacturing and Powder Bed Fusion

Additive manufacturing is a fabrication process that builds computer-aided design (CAD) models successively in thin layers of material. In advance, the 3D model is mathematically sliced and converted into readable machine code, and based on the process parameters, applied AM technology, and the material used, the software implementation (the code) is adjusted accordingly. The advantage of a layer-wise process such as this is the realization of intricate parts that previously would require an assembly of multiple parts and demand several conventional processes to achieve the desired geometry, which only accounts for the models that, in the first place, are feasible to fabricate using conventional methods. In other words, AM technology allows for highly customized and specialized parts without the limitations found in conventional methods. It can, even in small runs, be more economically viable as only the AM machine is required to produce the parts instead of a multitude of expensive tooling such as forms, punches, and dies. Additionally, there are no other manufacturing methods that have the same capabilities to go from idea to physical form in such a short time frame, hence the terminology: rapid prototyping (RP) and rapid manufacturing (RM). Although much of the primary interest in AM has been to visualize concepts and ideas, the introduction of functional AM fabricated metallic components has led to increasing interest in many sectors of the industry. For instance, the demanding requirements of lightweight and high strength design in aerospace and the automotive industry can be satisfied through AM, as the material is only added where it is needed, resulting in highly optimized parts for specific purposes. In like manner, medical and dental implants can be patient-matched through medical imaging in the biomedical sector, reducing the cost considerably [5, 13].

Of the metallic cellular structures produced through AM, approximately 90% of them are fabricated using powder bed fusion (PBF). More specifically, there are two types of heat sources for this type of AM technology: laser (L-PBF) and electron beam (EB-PBF). The former is the one adopted to produce the specimens for this thesis. Although there are some differences, the philosophy is quite similar. By using metallic powder, spread out with a given thickness over the build-plate, the highly localized and intense heat source consolidates the powder into a solid. In between the layers, the build-plate is lowered, and a roller spreads a new sheet of powder over previously built layers. This process is then repeated until the 3D model is fully built. This PBF process and its process parameters are better illustrated in Figure 4 and 5, respectively. Another key aspect of PBF manufacturing is the scanning strategies applied, where unidirectional, bidirectional, spiral, zigzag, and cross-wise are the most common ones. There are also strategies that involve changing the scanning direction for each successive layer to promote a more homogeneous strength throughout the part such that local strength does not mirror the scanning direction. Moreover, the scanning process is divided into two classes; the internal scanning termed hatch scanning and the contour scanning that follows the outer geometry as seen in Figure 6. Where the hatch scanning fills the interior with material, contour scanning is important to achieve smooth surfaces. Still, it is integral that these overlap, not to mention the bordering tracks of the hatch scanning, to ensure full melting.

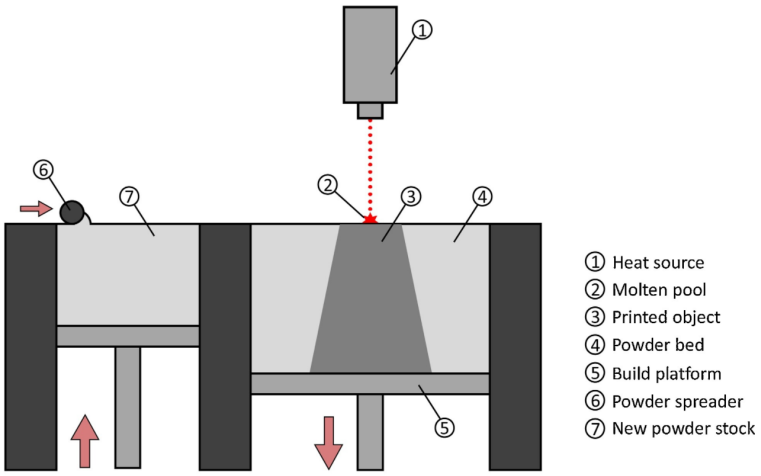

Figure 4: PBF processes [3]

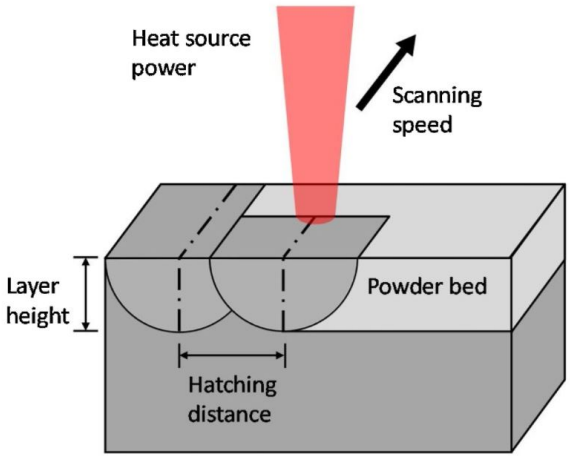

Figure 5: Process Parameters of additive manufacturing with PBF[3]

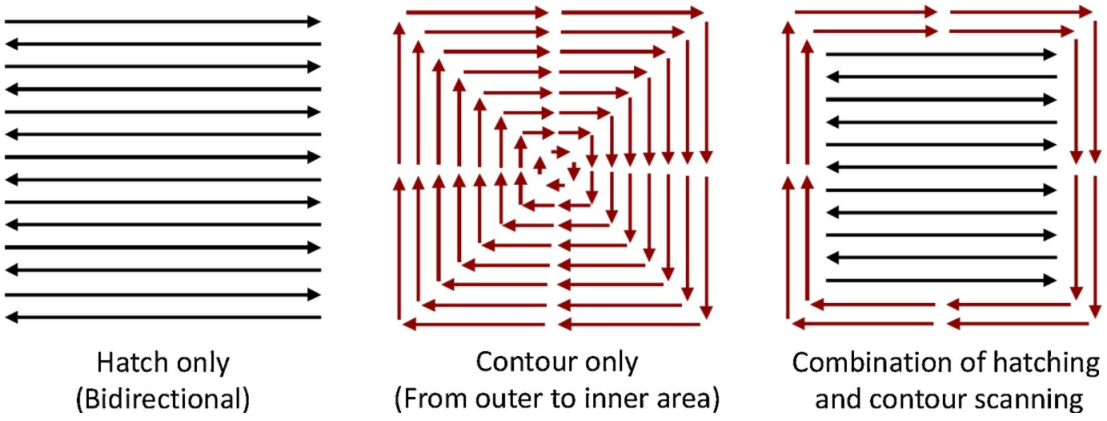

Figure 6: Various scanning strategies for PBF processes [3]

Despite many similarities, the laser and electron beam powder bed fusion processes are in many ways different. Whereas the L-PBF utilizes inert gasses such as argon and nitrogen, the EB-PBF process operates under a vacuum less than 0.01 Pa [26]. Another key difference is the layer height, where the L-PBF has a layer height ranging from $20 - 100\mu m$, and the EB-PBF has a notably higher range from $50 - 200\mu m$. Because of this, the precision between layers of the L-PBF is superior, resulting in finer and more detailed parts, which is crucial in the case of cellular materials. Similarly, the laser produces a smaller point of solidification in the powder between $30 - 250\mu m$ than the electron beam $200 - 1000\mu m$, which highly affects the accuracy and feasibility of producing smaller parts with satisfactory results. Another fundamental difference between the two heat sources is that, in contrast to the electron beams continuous focusing and supply of heat, the laser is driven by two independent parameters, namely the point distance and the exposure time. The point distance is the distance between points that the laser focuses on, and the exposure time is how long or short the focusing period is. In other words, the laser can be described as pulsating, whereas the electron beam focuses and apply heat in a continuous manner [30]. Evidently, both L-PBF and EB-PBF processes induce residual stresses due to the melt pools' high temperatures and rapid cooling. Hence, methods such as preheating the build-plate, preheating the powder, and various post-heat treatments of the printed parts are enforced to mitigate this effect. Here, another difference between the two processes arises. For one, L-PBF only preheats the build plate to approximately 200 degrees, unlike the EB-PBF process, where the powder bed is preheated to about 700 degrees by defocusing the electron beam. As a result of the high temperatures, the powder is slightly sintered, acting as a support structure around the solidified material. The benefit is threefold as this allows for better printing in overhang regions, faster-scanning speed, as well as stacking parts along the build direction with only layers of powder isolating them from one another [9, 30]. Although this may be true, the downside is that the powder can not be reused to the same degree as for the L-PBF process. Additionally, for porous, cellular materials, the slight sintered powder can get stuck in between the porous geometry, which defeats the purpose of the cellular materials altogether. Still, the EB-PBF produces parts in such a hot environment that rapid cooling of the solidified material is eliminated, rendering the residual stresses negligible compared to the L-PBF, which requires more post-heat treatments to reduce the residual stresses to an acceptable level. What is clear is that both processes have their pros and cons, but for manufacturing highly precise and detailed geometries at small scales, the L-PBF is the preferable choice. In Table 3, a comparison between the two powder bed fusion processes is highlighted.

Table 3: A comparison between laser and electron beam based PBF machines [30]

Parameters	**L-PBF (Realizer SLM50)**	**EB-PBF (Arcam EBM S12)**
Environment	Argon	Vacuum 10^{-2} Pa
Preheating (celcius)	200 (building table resistive heating)	700 (Powder bed heating by defocused electron beam)
Maximum beam power (W)	120	3500
Laser/electron beam spot (μm)	30-250	200-1000
Average powder layer height (μm)	20-100	50-200
Scan speed (m/s)	0.3-1.0	>1000

Even though AM technology has come a long way since its inception, there are numerous defects that are inherent to this complex fabrication process, mostly due to the high intensity and localization of the heat source but also that the quality of the manufacturing is influenced by a multitude of variables and parameters. Some of the typical defects are high surface roughness, porosity formation, unwanted microstructure (dendritic), residual stresses, micro-cracking, and poor dimensional accuracy between manufactured products and CAD models, just to mention a few. Since these defects are so consequential to the mechanical performance of the end product, optimal approaches to the process parameters, in-situ monitoring, post-processing, and other quality control processes have been well defined to minimize the extent of the defect and increase the reliability of the manufactured part [9]. For better insight, a few of the common defects and subsequent approaches are taken to mitigate these are addressed, specifically for AM through L-PBF. As residual stresses are unavoidable, especially in the case of laser additive manufacturing due to the highly concentrated heat source it generates, expansion and shrinkage occur in the material in proximity of the melt pool, often

labeled the heat-affected zone, which in extreme occasions can cause internal cracking. As such, it is now universally understood that these residual stresses can be mitigated or be close to insignificant by applying both pre and post-heat treatments of the material [27]. This also applies to improving the microstructure that for AM usually consists of inhomogeneous crystal structures of columnar crystal and fine dendrites. Here, a post-heat treatment will reorganize the microstructure to more of a typical homogeneous bulk crystal structure which in turn improves the mechanical properties [11]. There are mainly three ways they develop during fabrication when it comes to porosity. The first has to do with a lack of fusion due to insufficient energy applied, implying that more heat is required to fully melt the material. On the contrary, the second is due to excessive heat, which effectively vaporizes the metal, creating pockets of gas inside the solidified material. The third is due to poor overlapping of scan tracks which can leave some areas free of material. As such, the relation between energy output and scanning velocity in combination with optimized contour and hatch scanning path has to be carefully tuned such that neither too little nor too much heat is used and to ensure that the scanning paths satisfy complete melting between the tracks [9, 27]. The latter parts are especially difficult to achieve for lattice structures due to the fine feature size, as satisfactory scan strategies are harder to employ, given that only a handful of short tracks are required to complete a layer. In terms of surface roughness, it is most often a combination of varying thickness, inclination angles, and overhang regions, which also the scan strategies directly influence. In any case, as previously stated, these inherent defects are critical to the mechanical performance, but for fatigue strength, they are even more problematic as these defects already introduce cracks and high stress concentrations to the system, reducing the fatigue initiation life. In turn, only the propagation stage of the cracks remains, resulting in premature failure. This and more on fatigue will be further discussed in the following section 2.3.

2.3 Fatigue of Bulk Metallic Materials

Fatigue is the mechanism by which structural components are exposed to cyclic loading at stress levels below the given material's ultimate strength and yet are prone to failure. This can be explained by inhomogeneities in a metal, such as voids and particles of different chemical compositions, and the non-uniform nature of a microstructure, all resulting in an uneven distribution of the stresses. As such, there will be local regions within the material where the stress is higher than the material's ultimate strength, which causes microscopic damage. The cyclic loading then drives the accumulation of the microscopic damage resulting in nucleation and propagation of cracks and finally failure. There are also fundamental differences between ductile and ductile-limited metals when it comes to the process, damage, and failure characteristics. For a ductile engineering metal, the crystal grains with unfavorable orientation with respect to loading direction end up developing slip bands as the high shear motion between the crystal planes occurs, resulting in intense deformation. Additional slip bands are formed as more cycles are exerted on the material, and when reaching a saturation level, some individual slip bands become more acute, while others develop into cracks. As more of these are developed into cracks, they connect, producing even larger cracks that propagate to failure. On the other hand, for a ductile-limited metal, or so-called high-strength metal, the micro-damaging tends to be concentrated on preexisting material defects such as voids, inclusions, slip bands, grain boundaries, surface scratches, or other sharp flaws from the fabrication process. From these initial defects, small cracks develop due to high stress concentrations and grow in a plane normal to the tensile stresses until the crack grows large enough to cause failure or join other present cracks. In essence, highly ductile metals have a more widespread damage intensification, whereas the propagation of a few defects characterizes a high-strength metal [8].

It is common to differentiate between high cycle fatigue (HCF) and low cycle fatigue (LCF) when addressing fatigue life. This describes the number of cycles till failure at the applied stress levels and what type of deformation is occurring. For instance, in LCF, the stresses are high enough to cause plastic deformation during each cycle, different from the HCF, which only experience local plastic deformation. Accordingly, the accumulated damage for the two regimes will be quite different. The result of high stresses and plastic deformation of LCF is failure governed by crack propagation, while the low-stress HCF will be driven by crack initiation. Hence, it is usually more cracks and defects visible in HCF than for LCF failures as the HCF

forms new cracks, whereas LCF propagates from preexisting defects. As these regimes are determined by the type of deformation that transpires, there are no fixed transitions between them but are rather dependent on the ductility of the given material. Moreover, there are different models of evaluation for LCF and HCF. The former adopts strain-life fatigue models, performed under different strain amplitudes. Here, the Coffin-Manson relation, as seen in Equation 3 is the most frequently used stain-life fatigue model. In this relation, $\frac{\Delta\varepsilon_p}{2}$, ε'_f, $2N$ and C denote the plastic strain amplitude, fatigue ductility coefficient, number of reversals to failure, and fatigue ductility exponent, respectively. In contrast, the HCF utilizes a stress-based model to illuminate the expected fatigue life for a given applied cyclic load. By testing several specimens at various stress amplitudes; Basquin's relations, as seen in Equation 4; is then used for linear regression to provide the fatigue life data in a double logarithmic plot of stress and cycles till failure, more than often referred to as the SN curve. From Basquin's relation, σ_a, A, 2N, and B denote the stress amplitude, fatigue strength coefficient, number of reversals, and the fatigue strength exponent, respectively. Moreover, in Figure 7, a typical SN curve can be seen together with the two regimes of low and high cycle fatigue.

$$\frac{\Delta\varepsilon_p}{2} = \varepsilon'_f(2N)^C \tag{3}$$

$$\sigma_a = A(2N)^B \tag{4}$$

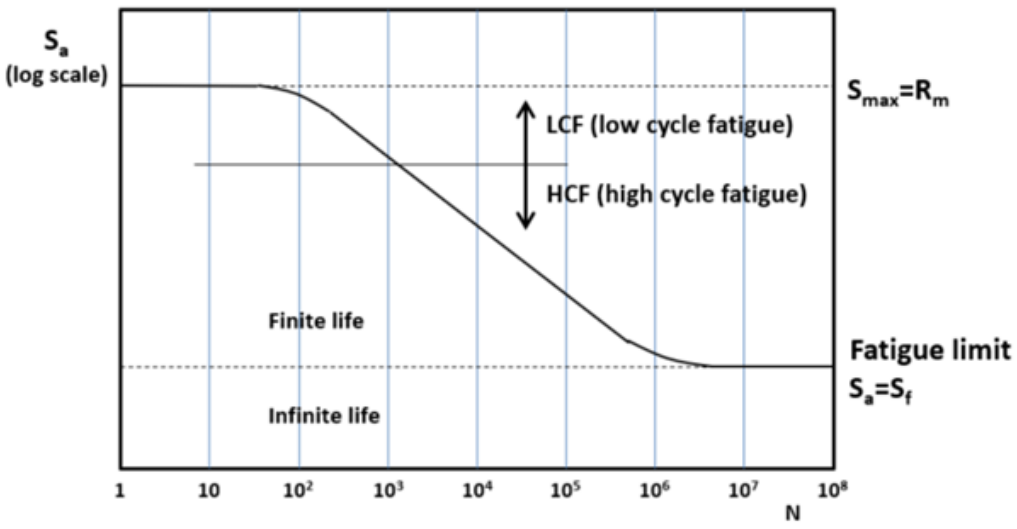

Figure 7: Typical SN curve [10]

2.4 Literature Review

2.4.1 Relative Density and Scale Effect

Yan et al. [32] evaluated the compressive strength and modulus of AlSi10Mg lattice structures for various volume fractions and unit cell sizes ranging from 7.5-15% and 3-7mm, respectively. The geometry design of the unit cell remained the same for all the specimens, namely a diamond structure, while the fabrication method used was direct metal laser sintering (DMLS). A clear relationship between volume fraction and cell size and the compressive strength and modulus was found. For one, the compressive strength and modulus increased as the volume fraction became larger. Alongside this, they reported that by also decreasing the unit cell size with a fixed volume fraction, the compressive modulus and strength would increase.

In another study, Yan et al. [34] investigated the microstructure and mechanical properties of AlSi10Mg with repeating gyroid unit cells fabricated via DMLS. They also compared how volume fraction and cell size ranging from 5-20% and 3-7mm, respectively, would influence the overall performance during the compressive tests. The specimens were also annealed for a duration of 2 hours at 300°Celsius. With respect to microstructure prior to the annealing process, it was evident that the melt pool was composed of two different zones in terms of grain size. In the vicinity of the boundary of the melt pool, the grain size of the dendritic microstructure ranged from 2-4μm, unlike the interior of the melt pool, which consists of a microstructure size of only 400-700nm. Moreover, the struts had relative densities of more than 99% as a result of the overlapping arc-shaped melt pools. Equally important was their finding from the compression tests. With a fixed volume fraction, both microhardness and compression strength decreased with the increase in unit cell size. This behavior was due to a higher cooling rate of the smaller unit cell sizes comprised of thinner struts, producing finer grains, consequently increasing the strength. Additionally, smaller dimensions provide a shorter scan vector which facilitates greater consolidation of the powder.

Similarly, Yan et al. [35] conducted tests on compression strength and modulus on 316L stainless steel with a TPMS gyroid fabricated through selective laser melting (SLM). In the same fashion, the volume fractions ranged from 6-12%, whereas the unit cell dimension stayed fixed at 5mm. They found that even the lattice structure with a volume fraction of only 6% was well manufactured and in accordance with the original CAD models. However, the struts at this scale were prone to very rough surfaces, which could possibly lead to premature failure if it was to undergo cyclic loading. This is consensual to their previous work, as they discovered that yield strength and Young's moduli both increased with the increase in volume fraction.

Much the same, Yan et al. [33] evaluated the performance of the same 316L stainless steel gyroid lattice structure fabricated with SLM. Here too, they found that cell sizes ranging from 2-8mm at a volume fraction of 15% could be manufactured with little to no defects, besides the many partially melted particles that are bonded to the surfaces of the struts. Still, this can usually be improved by grit blasting and various heat treatments. Furthermore, they discovered that the relative density of the struts varied with the cell size, where smaller cell sizes resulted in high relative density, which they argued was due to the shorter scan vector length and better wetting conditions when the cell size decreased. This also affected the yield strength and Young's moduli to the extent that the 2mm cell size had a 36% higher yield strength and 27% higher elastic modulus than the 8mm cell size counterpart, which is clearly an outcome of a higher strut density.

Continuing exploring the gyroid lattice geometry, Maskery et al. [21] explored the relationship between cell size and structural performance of double gyroid AlSi10Mg lattices manufactured with SLM. With the only varying parameter being the cell size, namely 3mm, 4.5mm, 6mm, and 9mm, they conducted a compression test on cubic specimens of 18x18x18mm. They found that different compressive failure modes were present for different cell sizes. The first mode of failure was the successive collapse of the cell layers perpendicular to the load and manufacturing direction, which only occurred for a couple of the 4.5mm and 6mm specimens. The second mode of failure was crack propagation perpendicular to the applied load and happened exclusively for the larger 6mm and 9mm cell-sized specimens. The last failure mode was diagonal shear which occurred

45 degrees to the loading direction and was almost entirely limited to the 3mm cell size specimens. In other words, smaller cell sizes are preferred as a way to mitigate low-strain failure due to crack propagation, although small cell sizes impose an entirely different set of problems if the smallest features of the lattice structure approach the manufacturing resolution.

Similar studies were conducted on SLM fabricated lattice structures made by stainless steel 316L, where the main focus was the behavior of the specimens in various loading conditions such as compression, shear, tension, and a combination of these. Gümrük et al. [14] also utilized different cell sizes ranging from 1.25-2.5mm and versions of the BCC lattice geometry, namely BCCZ that include vertical z-struts and F2BCC comprising of two BCC structures shifted 90°on each other. Similar to that of foam materials, the compression test for BCC and F2BCC geometries displayed a plateau region after the initial yield point, whereas the BCCZ geometry displayed peaks continuously after the initial yield point, although this effect diminished as the cell size became smaller. On the other hand, compression strength heavily favored the BCCZ structure, unlike the BCC, which proved to be the worst-performing structure. Regarding the shear tests, the many imperfections during manufacturing rendered the test very unpredictable in contrast to the compression test. Further, they found that the BCC structure cell size influenced what stress states were critical for plastic collapse. For the 1.25mm cell-sized specimen, the stress envelope that displayed compression vs. shear stress had an elliptical geometry, where the larger stress component was compression stress. On the contrary, the 2.5mm specimen saw no difference in the stress components; thus, the stress envelope was circular. Lastly, they found that the parameters that governed the mechanical response were relative density, unit cell geometry, and cell size.

Quit similar, a study conducted by Xiao et al. [31] compared three different lattice structures, namely Face Centre Cube (FCC), Vertex Cube (VC), and Edge Centre Cube (ECC) fabricated through SLM with 316L stainless steel. The geometries were also tested with various volume fractions ranging from 10-30%. From both numerical analysis and mechanical testing, it was evident that the FCC and VC cell geometry had superior mechanical properties in comparison to the ECC cell geometry. However, the ECC cell's efficiency in absorbing energy was much higher than the other structures, although the peaks in von mises stresses were also much higher. Conversely, they found that yield strength and elastic modulus plateaued when the volume fraction reached 30%, indicating an optimal strength to weight ratio for the cell size and geometries they tested for.

Finally, Mueller and Shea [25] considered how buckling, build-orientation, and scaling would influence the mechanical properties of small-scale 3d printed lattice structures approaching the printer's tolerance limits. The results displayed significant differences from both numerical studies and compression tests from their macro scale counterparts. Build orientation was crucial as effective diameters varied with the print strut angle due to the overhangs. This was more evident for smaller diameters as the layer thickness was fixed. They also found that the properties in the struts along the z-direction were weaker due to missing material. Still, as roughness is independent of the diameter, this effect diminished with larger diameters.

3 Method

3.1 Material and Specimen Preparation

The specimens used in this study were made by SLM solutions 280 in AlSi10Mg (material data sheet provided in Table 4), where the unit cell type is a sheet-based gyroid. The specimens fabricated were separated into seven different sets as seen in Table 5 which also outlines the various design properties for each set. The goal for these separate design properties was to differentiate them into three groups that isolated one parameter at a time. As described in Table 6, group A considers scale with constant porosity, group B considers the cube size with constant wall thickness, whereas group C considers wall thickness effect where the cubic size remains constant. As such, group A is a combination of the two latter effects. It should also be mentioned that A2 is included in all of the groups as the design combined aspects from each of the groups such that the number of sets required for the study was minimized from 9 to 7 sets. The as-built specimens captured by CT scanning can be seen in Figure 8 and 9.

Table 4: Material Data Sheet for AlSi10Mg [29]

Material Properties	**Values**
Density	2.67 g/cc
Tensile strength - Ultimate	264 MPa
Tensile strength - Offset Yield	151 MPa
Young's Modulus	57 GPa
Elongation at Break	19%

Table 5: Design Property Sheet for the Fabricated Sets

Lattice Name	**Cube Size [mm]**	**Unit cell size [mm]**	**Wall thickness [mm]**	**Porosity [%]**	**Amount of specimens**
A1	8	2	0.2	70.57	10
A2	25	6.25	0.625	70.57	10
A3	42	10.5	1.05	70.57	10
B1	8	2	0.625	31.52	10
B2	42	10.5	0.625	81.94	10
C1	25	6.25	0.2	90.19	10
C2	25	6.25	1.05	54.28	10

Table 6: Analysis Matrix

Group	**Parameter**	**Set**		
A	Scale w/ constant porosity	A1	A2	A3
B	Cube Size w/constant wall thickness	B1	A2	B2
C	Wall thickness w/ constant cubic size	C1	A2	C2

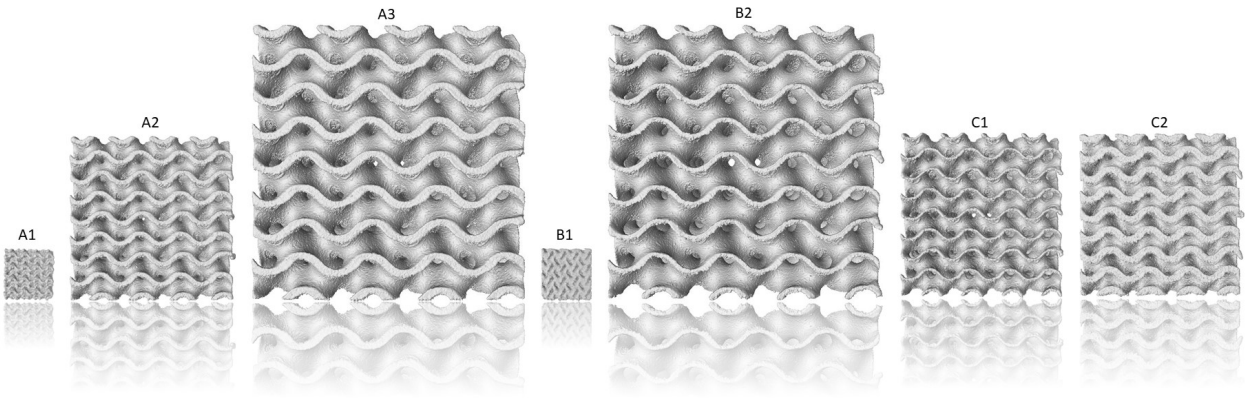

Figure 8: Side view of fabricated specimens

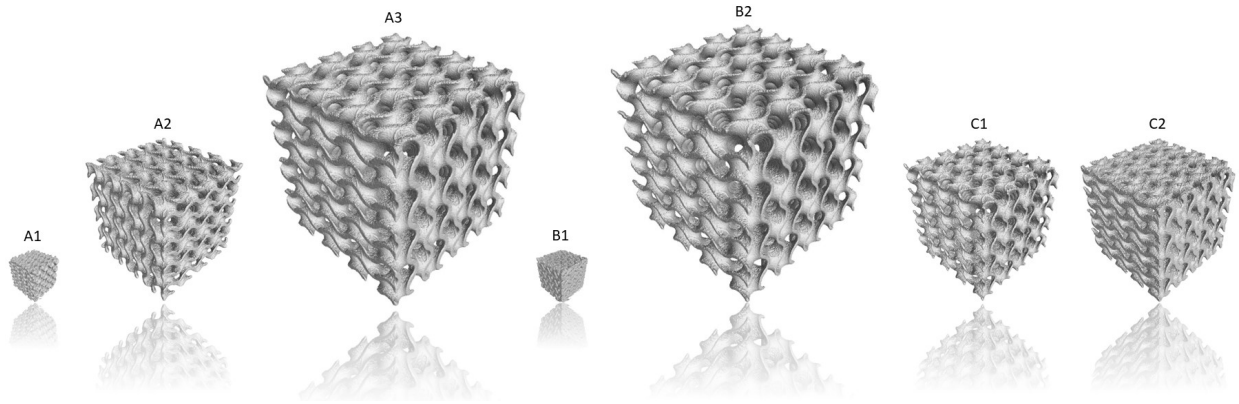

Figure 9: Bottom corner view of fabricated specimens

3.1.1 Dimensional Accuracy Analysis

The laboratory in Gjøvik that carried out the CT scanning used a GE nantomS tomograph. Due to size differences in the sets combined with the samples having to be within the field of view of the detector's field, they achieve different maximum resolutions for the various sample sizes. This resulted in a maximum resolution of 5.5μm for the 8mm specimens, 16μm for the 25mm specimens, and 27μm for the 42mm specimens. Moreover, the acceleration voltage was set to 160KV, in addition to filtering the beam through a CU filter with a thickness of 200μm in an effort to reduce the beam hardening. When it comes to the processing of the data, myVGL was utilized to find the new volume of the lattice structure. In this software, the iso-surface was set to roughly 130, that being the most centered grayscale value in the histogram before the new object volume could be obtained. Then based on the mathematical term for volume fraction as seen in Equation 5, a value for the total volume also had to be included. Seeing that the software did not accurately represent the total volume but rather the volume of the detector field from the CT scanning, the lengths along the three axes of the cube were instead measured. There was used three planes in each direction, one mid plane and two planes closer to the sides of the cube. Then each plane was sectioned into six different measurements divided upon the two axes of the plane. As a result, 27 measurements make up the new total volume of the cube.

$$\rho_{Actual} = \frac{V_{Object}}{V_{Total}} \tag{5}$$

3.2 Static Compression Test

The static compression tests were conducted on the Instron 8854 series, denoted as (A) in Figure 11, with a maximum load capacity of 250KN. The ultimate compression strain for each specimen was 50% of the original height. The displacement rate was based on the size of the specimen, which correlates to the 7% strain rate per minute of the original length. For the 8mm specimens, this meant a displacement rate of 0.57mm/min; for the 25mm specimens, this was increased to 1.78mm/min; and lastly, the strain rate for the 42mm specimens was 3mm/min. The details can also be seen in Table 7 Additionally, DIC images were captured every 500ms as a way to display the state of the lattice for different strains. The camera used for DIC was a VIC-2D v6, as shown in Figure 10.

Table 7: Displacement Rate for the Different Sets

Set	**Cube Size [mm]**	**Displacement Rate [mm/min]**
A1	8	0.57
A2	25	1.78
A3	42	3.00
B1	8	0.57
B2	42	3.00
C1	25	1.78
C2	25	1.78

Figure 10: DIC VIC-2D measurement system [4]

3.3 Fatigue Test

For the fatigue testing, a few different machines were utilized because of the large differences in the cross-sectional area of the specimens, i.e., the force required to reach similar stress states. The machine with the largest output was the Instron 8854 series 250KN, which was used on every set except for A1 and B1. A1

was tested on an Instron Electropuls series able to produce 10KN of force. Lastly, B1 and some retests of A1 were conducted on an Instron 1342 series with a load capacity of 100KN. These machines are shown in Figure 11. When conducting the fatigue tests, it was important to subject the specimens to stresses that could precisely cover the entire range of the SN-curve using linear regression. Moreover, to eliminate any unwanted errors and outliers, two specimens were tested for each input condition and assumed respectable if the number of cycles of both tests was in agreement. The force was calculated based on the relative density of the specimen as seen in equation 6, where F, σ, A_{cs} and $\bar{\rho}$ denotes the force, stress, cross-section, and relative density. Furthermore, the fatigue test was run in a compression-compression state with an R ratio of 0.1, including a runout limit of the experiment set to $2 * 10^6$ cycles. The load frequency of the machines was based on how stiff each subject was; hence the tests were conducted in the frequency range of 10 to 30 Hz. Another important aspect of the test was to place the specimens in the same direction compared to the build direction such that the bottom surface always faced the lower stage of the machine. Regarding gathering data during the fatigue tests, both the Instron 8854 and Electropuls series produce fewer data points for each logarithmic stage. The first ten cycles have data for each compression, then only every tenth cycle is reported until reaching 100 cycles. By then, only the 100th cycle will be reported till failure occur. However, with the Instron 1342, a data acquisition software called Catman was used to register and process the data. Since the test was running at 10Hz, the software was programmed to capture 50 points per cycle, in other terms, capturing in 500Hz. Then crucial data such as minimum displacement and force at each cycle was processed.

$$F = \sigma * A_{cs} * \bar{\rho} \tag{6}$$

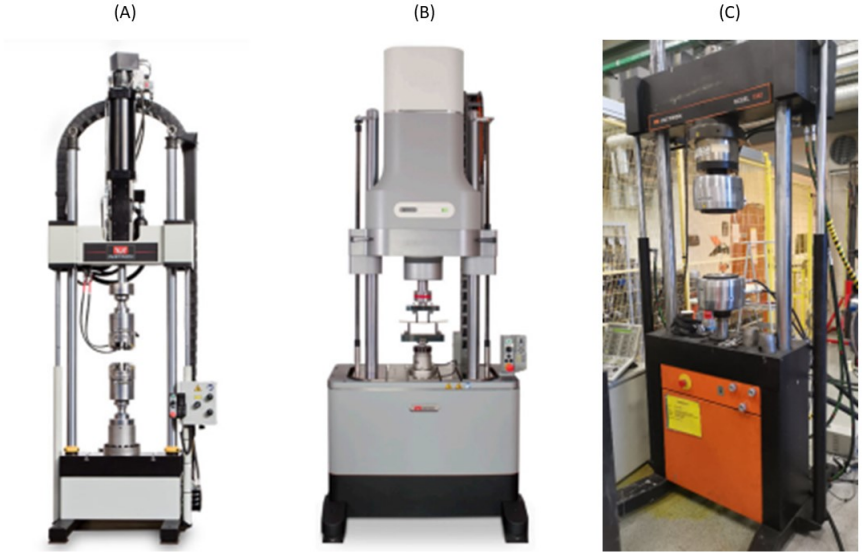

Figure 11: (A) Instron 8854 - 250KN, (B) Instron Electropuls - 10KN and (C) Instron 1342 - 100KN

The stiffness vs. cycle plots was obtained by using the equation for a spring constant, as seen in Equation 7. In the calculations, F is the Max load during full compression, whereas the deformation length L is the maximum displacement at each recorded cycle; in other terms, when the specimen is in the most compressed state. As such, the max load and used deformation length should correlate, seeing that the highest compression state is only attainable through a corresponding force, i.e., max force equals max displacement.

$$K = \frac{F}{L} \rightarrow \frac{N}{mm} \tag{7}$$

3.4 Failure Assessment

For capturing the fracture locations and close-up imagery of surface roughness, the SEM - QUANTA 650 FEG was used, as seen in Figure 12. The preparation process placed the samples in glasses filled with ethanol and then proceeded with approximately 5 minutes of the ultrasonic bath. This was to ensure that nonconductive particles such as dust were removed from the specimens to avoid trapping electrons, ultimately making for poor images. Similarly, the beam voltage was set to 22kV as this produced the finest images with the least amount of dark vignette.

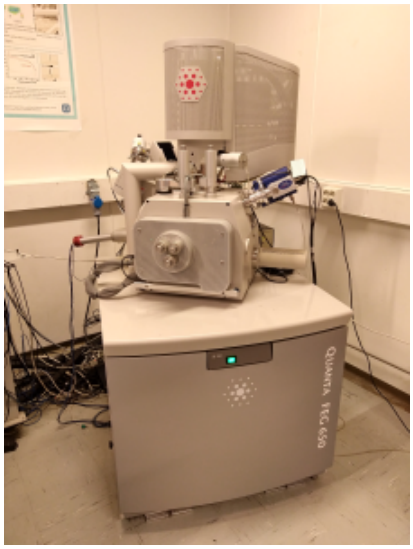

Figure 12: SEM - QUANTA 650 FEG

3.5 Micro-Structural Analysis

The specimens were also grinded and polished to prepare them for chemical etching, where grain size and grain boundaries could be analyzed with both an optical (Olympus BX53M) and digital microscopy (Hirox rH-2000), illustrated in Figure 13. The grinding was carried out in four stages with grit sizes p120, p500, p1000, and p4000, followed by two polishing stages at 3 and 1 microns, respectively. The amount of time for each stage varied, although if any scratches were visible in the polishing stage, either more time was spent on polishing with 3 microns or previous steps were revisited. When the surfaces were sufficiently smooth, the specimens were sent to chemical etching. The chemical composition called Kellers's etchant was composed of 190ml of distilled water, 5g of nitric acid, 3ml of hydrochloric acid, and 2ml of hydrofluoric acid. However, the analysis was never finalized due to the time limitations of the lab responsible for the chemical etching.

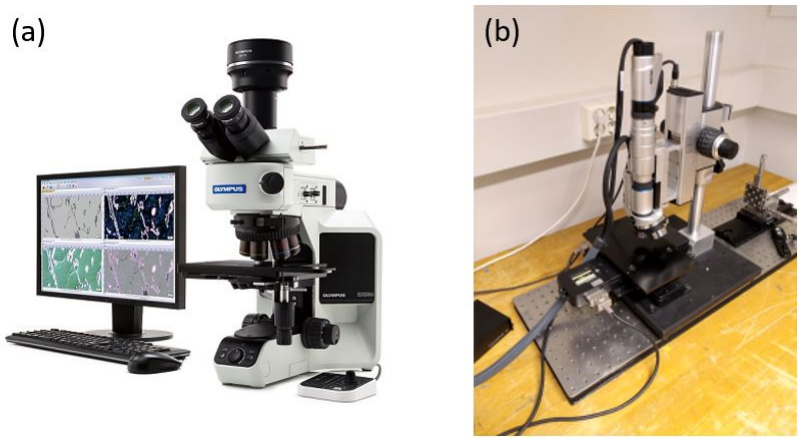

Figure 13: Optical (a) [28] and digital (b) microscope

4 Results and Discussion

In this chapter of the thesis, the results are reviewed and discussed. First, the dimensional accuracy of the fabrication process is investigated with the data provided by the CT scanning. Next, the stress-strain plot for the static compression test is analyzed, which incorporates both the designed and actual porosity of the specimens and eventually a normalized plot based on the newfound yield strength. Similarly, the fatigue looks at what differences arises when the actual porosity is accounted for, followed by a thorough comparison between group A, B, and C, being scale effect, cube size effect, and wall thickness effect. Finally, the failure mechanics through digital microscopy and SEM is reviewed, both in terms of global and local failure location, not to mention the surface topology at critical locations.

4.1 Dimensional Accuracy

In this section, the dimensional accuracy of the fabricated specimens and the internal porosity of the bulk material are investigated. Without delay, Figure 14 illustrates the discrepancy between the intended volume fraction of the specimens and the volume fraction calculated based on the results from the CT measurements. Additionally, by including the scale of the specimens in the x-axis, a relationship can be seen as the dimensional accuracy is clearly dependent upon the scale of the fabricated part. For instance, the deviations are 4.46% and 3.40% for sets A3 and B2, with the largest cube sizes. The second-largest cube size of 25mm featured in sets A2, C1 and C2 have a more significant deviation of 7.34%, 8.67%, and 9.25%. Conversely, at the minor scale of 8mm, the dimensional accuracy is exponentially weaker, not to mention the significant difference in accuracy between the two fabricated sets at this scale. A1 is roughly 38.03% denser, followed by B1, which is nearly 47.11% denser than the intended geometry. These details can also be seen in Table 8. As Yan et al. argued [33], specimens of smaller scales have a higher strut density than intended because of a shorter scan vector length and better wetting conditions.

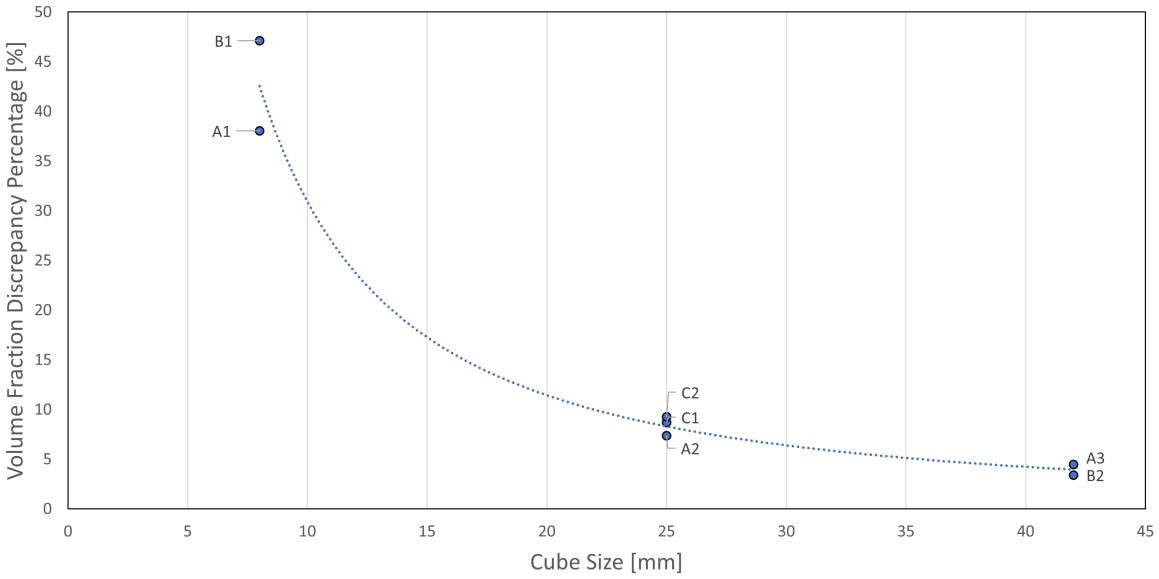

Figure 14: Discrepancy percentage between designed and actual volume fraction

Table 8: Details Surrounding the Intended and Actual Volume Fraction

Set	Cube Size [mm]	Porosity [%]	Actual Porosity [%]	Discrepancy Percentage [%]
A1	8	70.57	43.72	38.03
A2	25	70.57	65.38	7.34
A3	42	70.57	67.42	4.46
B1	8	31.52	16.67	47.11
B2	42	81.94	79.15	3.40
C1	25	90.19	82.36	8.67
C2	25	54.28	49.25	9.25

4.2 Static Compression Analysis

In this section, the stress-strain curves are analyzed and compared to indicate the individual stiffness, yield strength, compliance, and how the progressive damage of the specimen unfolds. Here, all the specimens were compressed to 50 percent of their original length with a strain rate of roughly 7%. Due to variation in designed and actual volume fraction, as previously stated in Section 4.1, two instances are displayed instead. The first one is Figures 15 and 16 where the stress is calculated based on designed porosity. The other in Figures 17 and 18 where the actual porosity found thorough CT scanning is being accounted for. It is noteworthy that the initial discrepancy in applied stress is because of surface roughness and support structures. Based on these results, an estimate of the yield strengths in combination with a normalized strain-stress plot is presented as seen in Table 9 and Figure 20, respectively. Lastly, the pictures measured with the DIC camera are compiled in Figure 21 which includes keyframes at strains between 0 and 50%.

The first of these plots seen in Figures 15 and 16 demonstrate a variation between the sets in all of the regimes, including the linear elastic regime, the stress plateau, and the densification stage. First and foremost, both A1 and B1 are the sets that provide the smallest unit size of only 8mm. What seems to be the case at this certain scale is a much higher initial yield strength at approximately 230MPa when compared to the other sets that range between 100-150MPa. This is followed by a gradual increase in stress during the stress plateau regime, which lasts about 30 to 40% strain. The stress rapidly increases as the inside structures become more compact during the densification stage. Although both A1 and B1 follow almost the exact same path in the linear elastic regime, the latter diverges at a lower compressive strain because of solidification, as can clearly be seen in figure 21. The fact is that with less room inside the geometry, the amount of strain required until neighboring interior geometry makes contact will shorten. In the plot, these are the rapid incline in stress after yielding, A1 admittedly not occurring until a higher strain has been reached. This is because of the higher porosity found in A1, which allocates more space in the interior before eventual collisions occur, compared to B1.

A2 and A3 have very similar curves, although offset by a minor factor in stress. After initial yielding, they both have a small collapse seeing that the stress shows signs of falling in the plateau regime. Subsequently, there is an increase in stress again during the later stages in the densification stage. That said, A2 and A3 have a higher porosity which likely leaves enough space in the interior geometry to mitigate any significant contact. Another critical point to mention is that the material (AlSi10Mg) or geometry is relatively ductile as there is no significant variation in stress in the plateau regime due to sequential collapse of the structure, more commonly seen in a brittle material. Still, some minor sequential collapses for two of the sets feature a higher porosity, resulting in a thinner geometry more susceptible to these collapses. The implicated sets being B2 and C1, the former only having one slight collapse between 25% to 30% strain before recovering, and the latter seemingly having two collapses. The first is the more significant collapse of the two, occurring in the range of 15% to 25% strain, which recovers to initial plateau stress at roughly 33% strain. The second occurs right after recovery, but now with a smaller drop in stress than the first one, not to mention a moderate

recovery in comparison. Lastly is set C2, which performed exceptionally well in yield strength for the sets with the same and larger unit sizes. Similar to A1 and B1, C2 provides a lower porosity of 54%, presumably why the plateau regime has no rapid declines in stress and an increase in stress during the densification stage due to internal collisions.

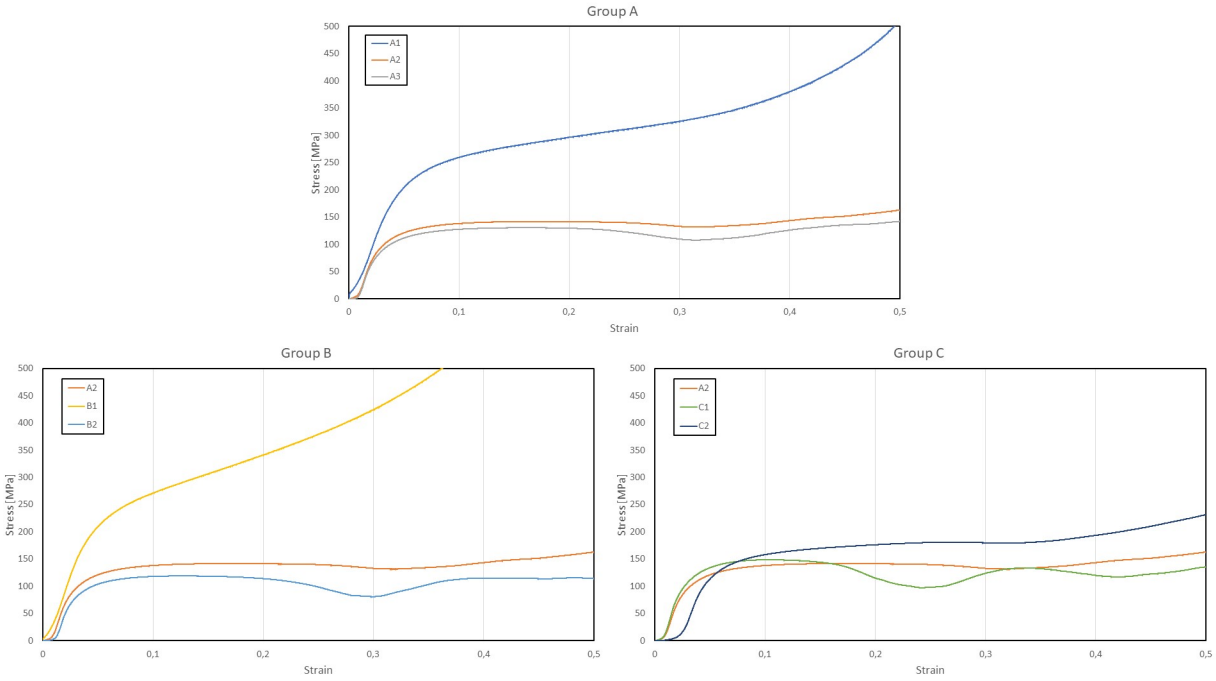

Figure 15: Stress-Strain curves based on intended design parameters, split into the groups

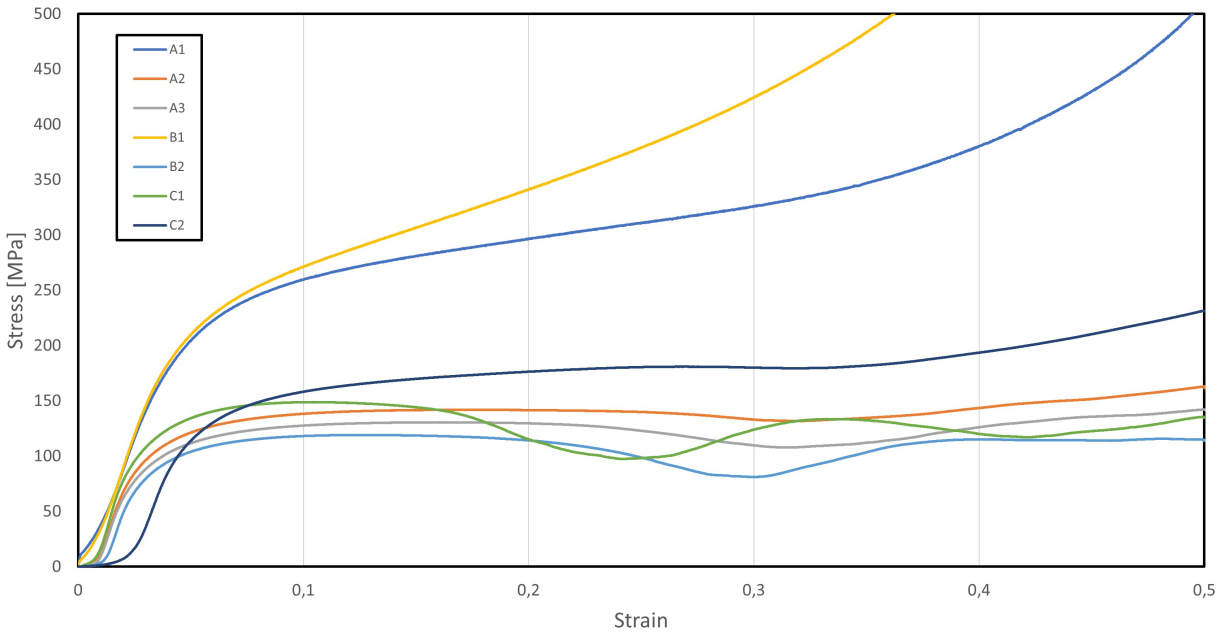

Figure 16: Stress-Strain curves based on intended design parameters

Basing the stress on the newfound values for the cross-sectional area through the CT measurements, there is now a convincing and universal drop in stress throughout all the sets, better illustrated in Figures 17 and 18. Firstly, B1 seems to be a case where a much higher yield and progressive increase in stress throughout the plateau regime occurs because only a tiny amount of compression is required to have a bulk material essentially. For this reason, changing the theoretical volume fraction to the actual volume fraction still makes B1 an outlier, provided that a lattice structure and solid material do not behave similarly. Surely compressing a lattice for 0.5% strain is not the equivalent of compressing a solid for the same amount of strain. Conversely, A1 seems to readjust and now correspond well with C2. This is likely an outcome of the similar volume fraction for these, with A1 having a porosity of roughly 43.72%, whereas C2 is slightly higher at 49.25%. Seeing that porosity governs both yield strength and the subsequent plateau and densification regimes, it may be that the lower porosity contributes to larger wall thicknesses. As a product, there are earlier signs of contact within the structure. This solidification will bring about a stiffer material and conjointly increase the force required to further compress the lattice structure. The figure shows that the amount of strain before the densification stage commences is heavily influenced by the porosity. On the other side of the spectrum, the lower porosity sets B2 and C1 have changed roles in that B2 is now stronger than C1. After all, the adjustment closed the gap in volume fraction between them as B2 is roughly 79.15% and C1 is slightly larger at 82.36%. This seemingly small variation between them in porosity still counts for approximately a 22% difference in yield strength. Lastly, A2 and B2 are even more similar in strength than they already were. Besides a small dip in stress for A3 when approaching 25% strain, the variations are negligible.

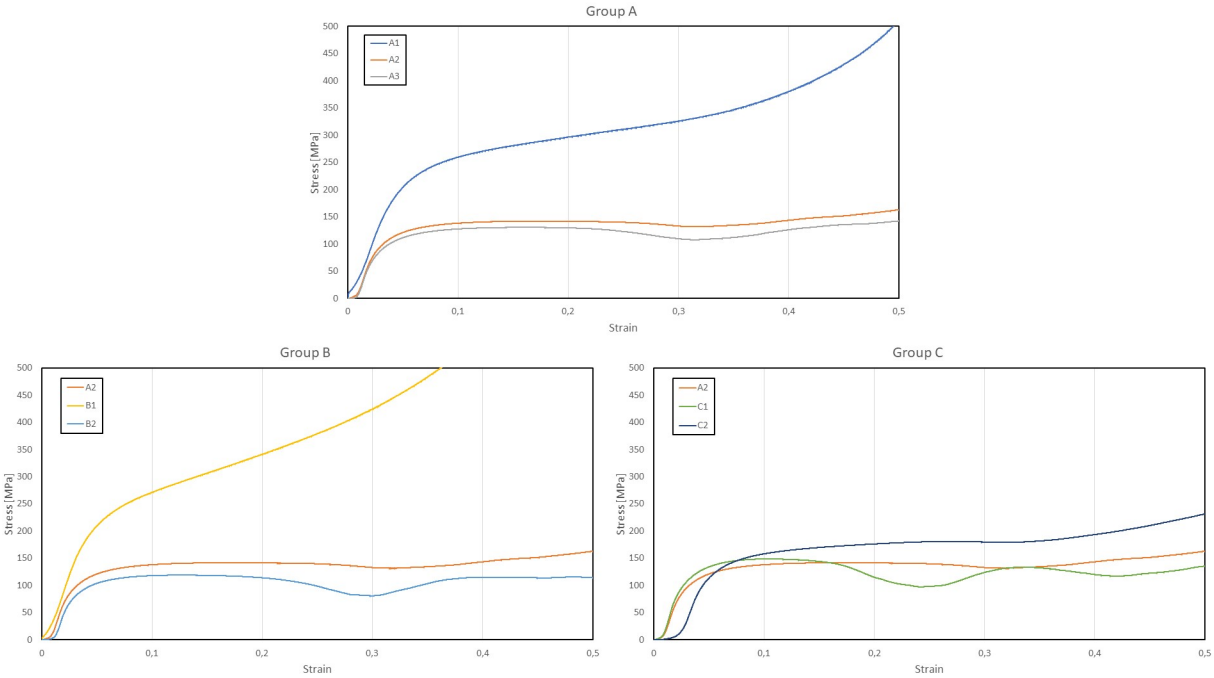

Figure 17: Stress-Strain curves based on actual fabricated parameters, split into the groups

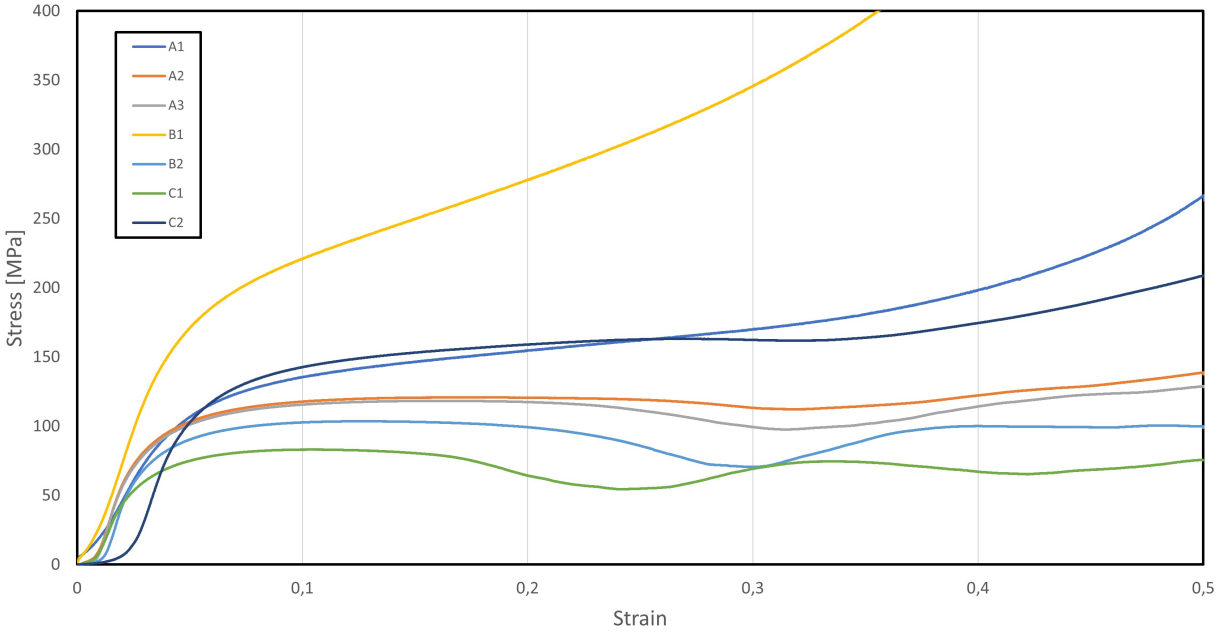

Figure 18: Stress-Strain curves based on actual fabricated parameters

All things considered, the most prominent trend for this stress-strain plot is the relation between volume fraction, scale, and the strength of the material. As pointed out, a lower porosity will increase the strength even though the cross-sectional area is accounted for, and at smaller scales will lead to premature contact of the interior geometry, which also aids in strengthening the lattice. The yield strength for each set has been calculated based on the 0.2% offset rule and is shown in Table 9. Here, the yield strength appears to follow the porosity except for A1 and C2, indicating that also scale may be significant. In any case, these results are similar to what Yan et al. discovered [33] in that strength increases proportionally to the volume fraction. For the last stress-strain plots in Figures 19 and 20, the stress has been divided by the yield strength. The different behavior for cube sizes and porosity previously discussed is even more explicit. Ranging from the earlier densification of A1, B1, and C2 to the more porous behavior of B2 and C1 that show significant drops in integrity in the plateau region. In many ways, the sheet gyroid geometry behaves more stretched or bending-dominated depending on the porosity and scale. Besides this, the yield plateau is quite similar between the sets, although it is A3 that displays the highest one.

Table 9: Yield Strength and Young's Modulus Based on 0.2% Offset Rule

Groups	**Set**	**Yield Strength [MPa]**	**Young's Modulus [GPa]**	**Porosity [%]**	**Cube Size [mm]**
	A1	120.2	2.959	43.72	8
Group A	**A2**	101.6	5.226	65.38	25
	A3	89.3	5.565	67.42	42
	B1	190.5	4.93	16.67	8
Group B	**A2**	101.6	5.226	65.38	25
	B2	89.5	5.172	79.15	42
	C1	72.9	4.023	82.36	25
Group C	**A2**	101.6	5.226	65.38	25
	C2	126.3	4.908	49.25	25

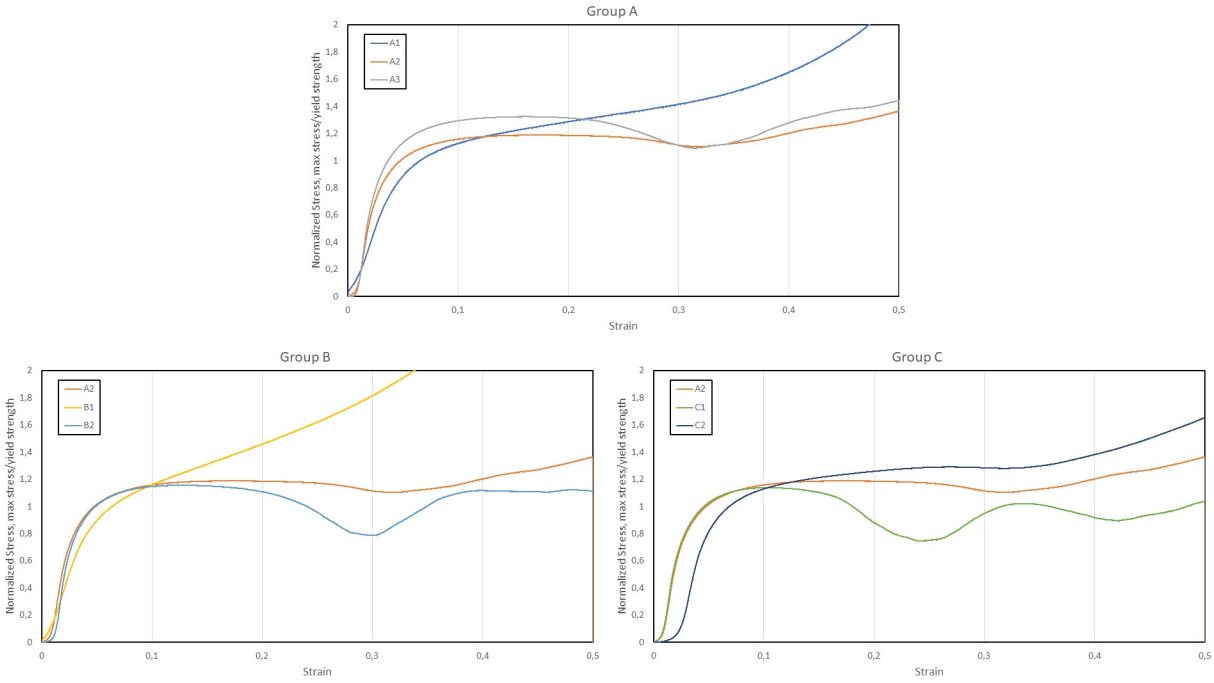

Figure 19: Normalized Stress-Strain curves based on yield strength, split into the groups

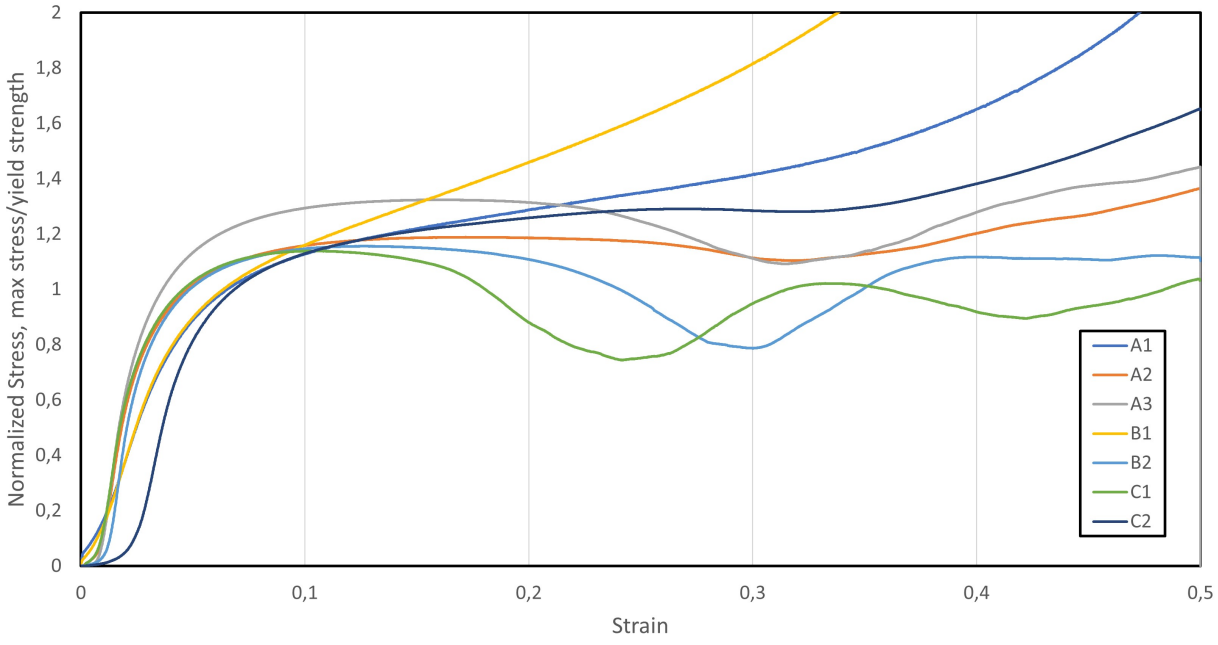

Figure 20: Normalized Stress-Strain plot based on yield strength

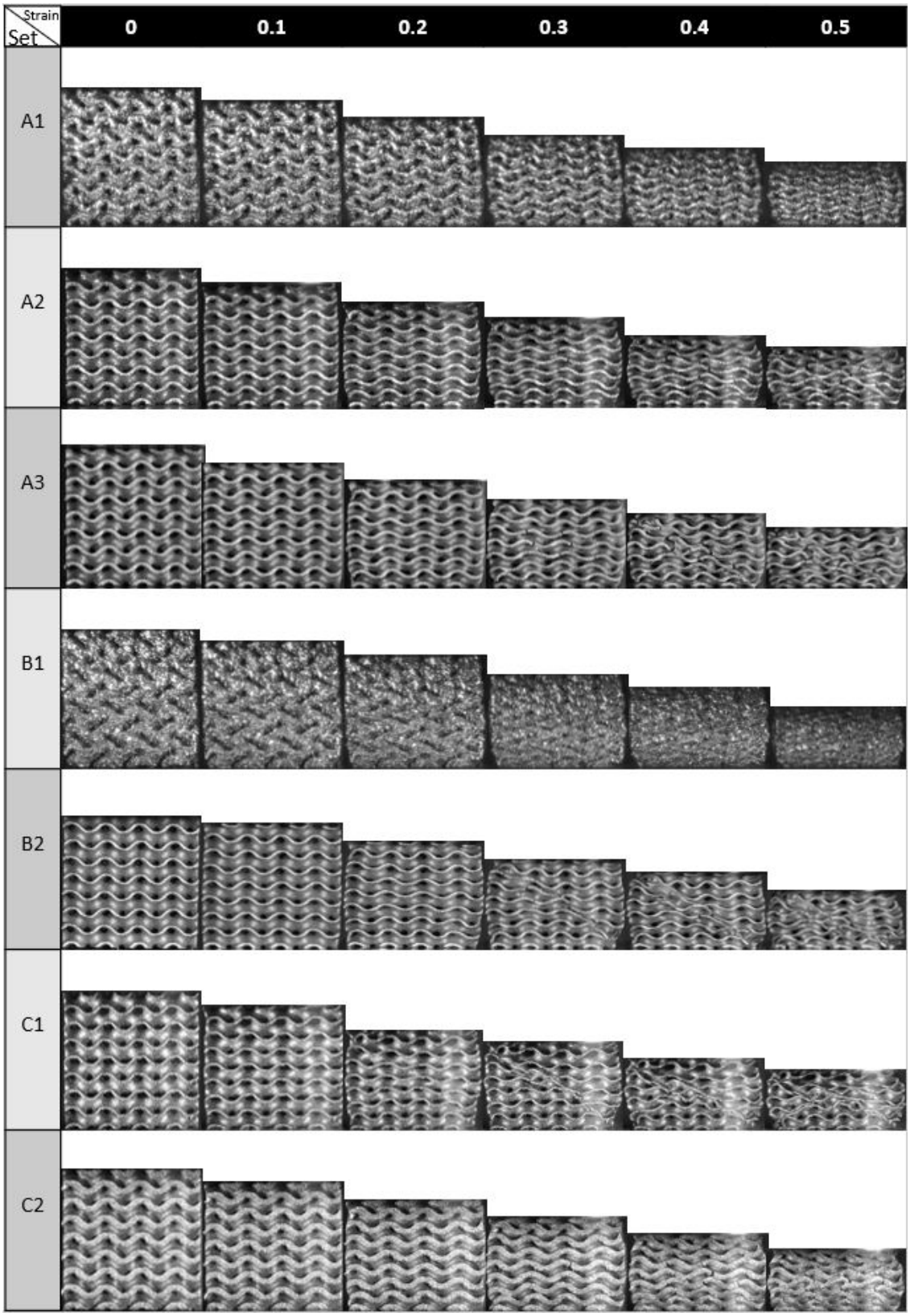

Figure 21: Gradual deformation of the lattice structure

4.3 Fatigue Results

In this section, the topic of conversation will be the fatigue behavior of the tested specimens. By differentiating the sets into three different groups as presented in the analysis matrix in Table 6, a relationship based on the individual exercised effects such as scale, cube size, and wall thickness effect can be detected. In reviewing and defining the influence of these effects, SN plots and normalized SN plots with the newfound values for yield strength are presented utilizing actual cross-sections, followed by a plot outlining the progressive stiffness loss throughout the fatigue life for both regimes of LCF and HCF. The tests chosen to display the stiffness are based on similar cycles to reach failure in both instances. At the very end, the results for each group are combined, and a brief evaluation of the fatigue behavior is taken. It should be noted that low cycle and high cycle fatigue will be mentioned several times in this section, but unlike the original terminology of LCF and HCF from section 2.3, this section refers to these entities in the way of differentiating the earlier and later stages of the fatigue life with no exact number of cycles.

4.3.1 Scale Effect with Constant Porosity

The first category explored is the scale effect with constant porosity, including sets A1, A2, and A3, which combines the effects of cube size and wall thickness that will subsequently be discussed. In terms of the constant porosity, it was predetermined to be roughly 70.57%, although the actual values measured from the CT scanning were 43.72%, 65.38%, and 67.42%, respectively. Still, the cube size remains the same, 8mm for A1, 25mm for A2, and 42mm for A3. When considering the SN curves of these sets illustrated in Figure 22, it is clear that between the three sets, there is one considerable outlier, being set A1. To emphasize, where only 81 and 85 MPa is required to reach failure for A3 and A2 at roughly 100 thousand cycles, the same amount of cycles till failure is reached when A1 is loaded with approximately 115MPa. Under those circumstances, A1 seems to have approximately 1.35 times the capacity against fatigue than the two larger specimens in the LCF regime. That said, there are inherent issues when manufacturing geometries in the miniature scales that A1 possesses. From what can be gathered from the CT scans of the specimen in group A1, the actual porosity differs by 38%. As such, the compression mechanics during the fatigue life of the structure will be different than in the case of A2 and A3, much like how they differed in the strain stress plots in section 4.2. Concerning A2 and A3, they seem to operate similarly, although there are minor differences in load levels as projected in the last illustration that combines the three sets. To demonstrate, at 10 thousand cycles, A2 and A3 fail at 95MPa and 93MPa, that being just a 2% difference. However, in the higher regimes of the fatigue life, this variation grows larger to the extent that at 1 million cycles, A2 reaches failure with a stress of 73 MPa, and A3 fails with the stress of 68MPa, which is a 7% difference. In essence, A2 seems to withstand slightly higher stresses than A3, which again reinforces better fatigue resistance with smaller scales, admittedly with a smaller variation between A2-A3 than A1-A2. Still, this trend is likely because a larger specimen has a smaller variation between modeled geometry and the produced part, seeing that the inherent roughness that materializes with this type of manufacturing affects the overall volume fraction for smaller-scale specimens more than larger specimens. Consequently, a smaller specimen will have a larger cross-section than its scale, which proves beneficial for a long fatigue life as more propagation of the developing cracks is required for failure to occur. As for the fatigue limits acquired through regression, the ranking between the sets remains the same. A1 is still the strongest with a fatigue limit of 84.7MPa, followed by A2 at 71,14MPa, and lastly, A3 with a fatigue limit of 66.8MPa. To emphasize, this means that A1 has a 19% higher fatigue limit than A2, whereas A2 has a 6% higher fatigue limit than A3. In terms of the runouts from the testing, both A2 and A3 were seemingly close to this limit, with the former meeting the runout condition at 68MPa and the latter at 63MPa. For A1, the runout reached 73.2MPa, albeit with more capacity to increase the load and yet last for more than 2 million cycles.

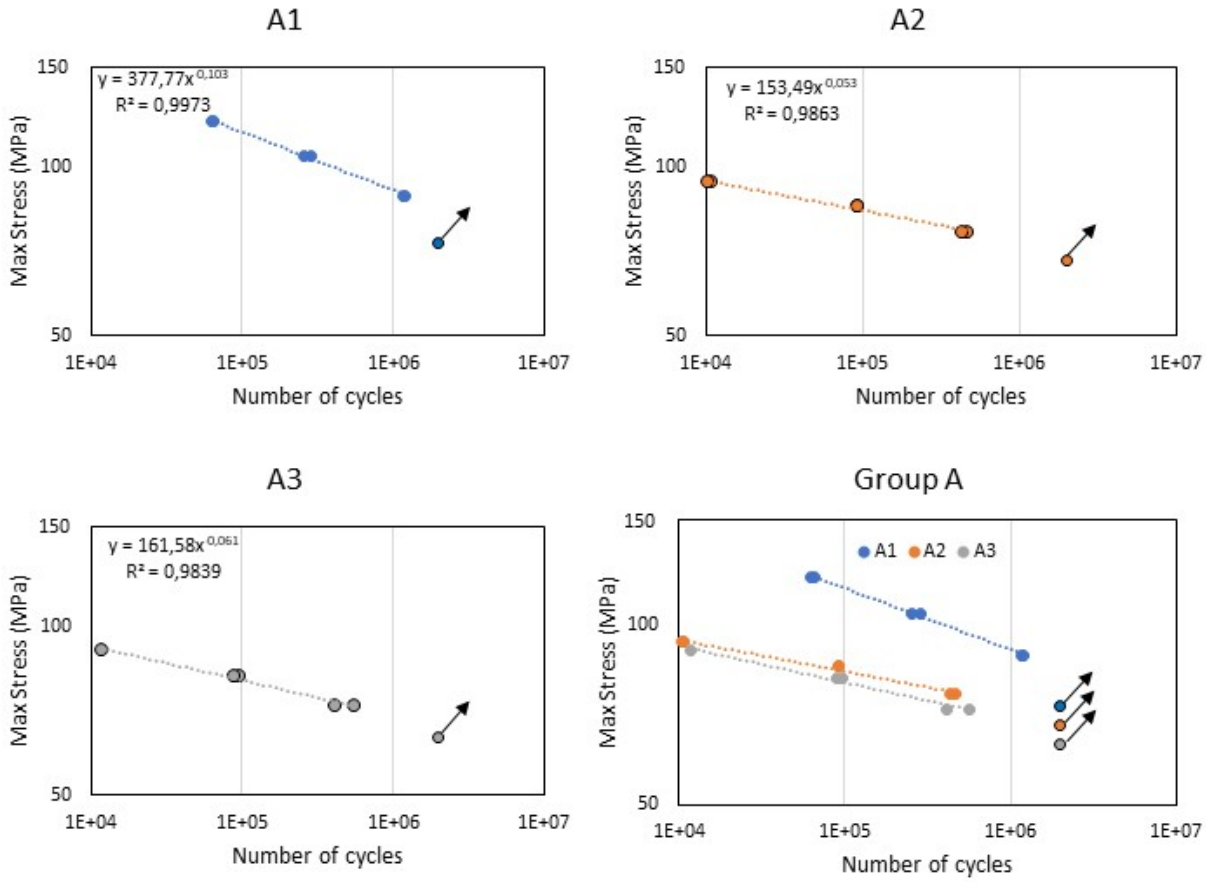

Figure 22: SN Curve - scale effect with constant porosity

Seeing that the variations between the three geometries have more to do with the limitations set by the manufacturing method than what the theoretical scale effect by itself would contribute in terms of fatigue life, a normalized plot based on the yield strength is also provided as seen in Figure 23. Since the yield strength incorporates the porosity, this plot effectively illustrates the curves as if the porosity were the same. Conversely, the compression mechanics of the denser lattice structure such as A1 still behave differently than A2 and A3, which closely resembles the designed porosity, hence the steeper slope for A1. In any event, the normalized curve displays the pair of A2 and A3 switching places with respect to stress required to reach failure, whereas A1 still shows a preponderant ability to withstand fatigue failure in the low cycle fatigue regime. At approximately 10 thousand cycles, A2 reaches failure when loaded with 92% of its yield strength, whereas A3 is loaded with roughly 101% of its yield strength. By the same token, when A1 is loaded with the same stress as its yield strength (100%), the failure occurs when reaching roughly 60 thousand cycles. Due to the steeper slope of A1, the fatigue strength beyond approximately 500 thousand cycles becomes worse than that of A3. This is particularly reflected in the fatigue limits as A1, A2, and A3 are reaching this limit when loaded with 70%, 69%, and 75% of its yield strength, respectively. That means that A1 is barely stronger than A2, and even more so with respect to A3. Still, with only 6% variations across the sets, the fatigue limit is similar now that the yield stress is accounted for. Given these considerations for both the low and high cycle fatigue regime, there is a convergence amongst A1 and the two other sets when approaching the fatigue limit, subsequently a similar slope progression of the other pair. This means that under LCF, the sets are more sensitive to the fabrication process in that the unit size decides the amount

of extra material which is added. Thus, a smaller unit size will have a larger wall thickness in relation to both the length of the struts and the unit size. On the other end of the spectrum, the extra material matters less when lower stress is imposed as this regime is mainly governed by elastic deformation, developing from the imperfections and forming new cracks, and not high plastic deformations, which generally propagates a couple of the preexisting cracks till failure. Using the same example as before, the lower loads and mostly elastic deformation will not propagate preexisting cracks to the same extent as higher loads, which would be quite detrimental for struts that are thinner in relation to the unit size.

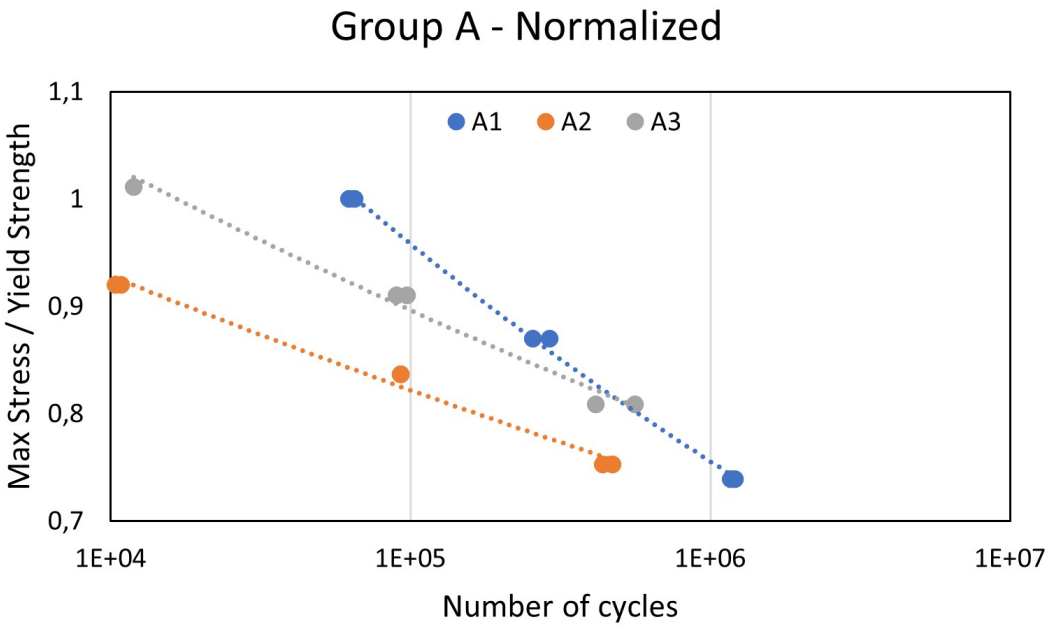

Figure 23: Normalized SN curve for group A

Equally important is the progressive stiffness loss through the fatigue lifespan. In this analysis, similar cycles till failure were chosen, one for the lower fatigue regime and one for the higher fatigue regime, as illustrated in Figure 24. With porosity staying the same and the cube size fluctuating for the different sets, it is expected that the force and displacement, being the two components in calculating the spring stiffness, is scaling to one another. In other terms, a larger unit cell assumes a larger cross-section, a higher force to meet the same stress state, and a more significant displacement to meet the targeted displacement percentage of 20%. That said, the test on A1 was completed on another fatigue machine than the other sets, which used approximately ten thousand cycles to reach the intended load amplitude, whereas A2 and A3 reached this within ten cycles. This influences the stiffness for A1 so that it is much more gradual than the two others meaning that the stiffness is more comparable following 10 000 cycles till failure. Hence, this is verily the first point of interest concerning A1.

With respect to the first of the three plots, sets A2 and A3 reach cyclic softening faster than A1 and then lose stiffness more rapidly when reaching this stage. Conversely, A1 retains more stiffness for a more extended period. However, after transitioning to cyclic softening, the change in stiffness is minuscule in comparison, which is ordinarily more typical for bulk materials. What can be said about the varying change in stiffness between the three sets is that for larger specimens, there is a more rapid loss in stiffness throughout the fatigue life, whereas, for the smaller specimen, the change in stiffness is more limited. With attention to their relative densities, this really means that for A1, the densification of the structures aid in retaining the

stiffness, and for a more porous structure such as A2 and A3, the structure will more easily comply and deform. Moreover, both A2 and A3 vary in stiffness, although they seem to converge the closer it comes to failing. Evidently, there is no rapid decline at the end of the fatigue life for any low cycle fatigue tests due to an overwhelming amount of cracks formed in the specimens, rather consistent plastic deformation that promotes enough deformation to meet the displacement requirement of 20%. This is especially true for A1 which there is little to no fall in stiffness when reaching failure. When evaluating the second plot of the high cycle fatigue regime, it is clear that there is less compliance for all the sets as the displacement does not scale with the decrease in load. Still, there are some similarities in the initial loss in stiffness amongst A2 and A3, unlike A1, which suggests requiring more cycles to stabilize, although this has primarily to do with the machine. The steepness during cyclic softening is also quite similar to before in comparison to each other, despite a higher offset between them. Concerning A2 and A3, the latter retain more stiffness throughout the fatigue life even though these specimens last for roughly the same amount of cycles. In the same fashion, A1 seems to maintain the lowest stiffness out of all the sets, at least after transitioning to cyclic softening. Furthermore, the sets correspond with the theory of high cycle fatigue in that there is a rapid loss in stiffness in the concluding stages of the fatigue life. As an abundance of cracks develops in the lattice through local plastic deformation, small individual fractures are forced to form in the features of the lattice structure. In summary, it is an unmistakable trend in stiffness loss connected with the effect of scale. In all instances, larger sizes also provide a higher stiffness. This can simply be explained because more material is compressed whenever the size increases. On the other hand, the curve's steepness is an entirely different case that is grounded in the deformation mechanics at different strains. For A1, the packing of material aided in keeping the stiffness constant. At the same time, the more porous structure was not restrained to the same degree by its neighboring geometry, which leads to thinner and longer struts more prone to buckling and fractures.

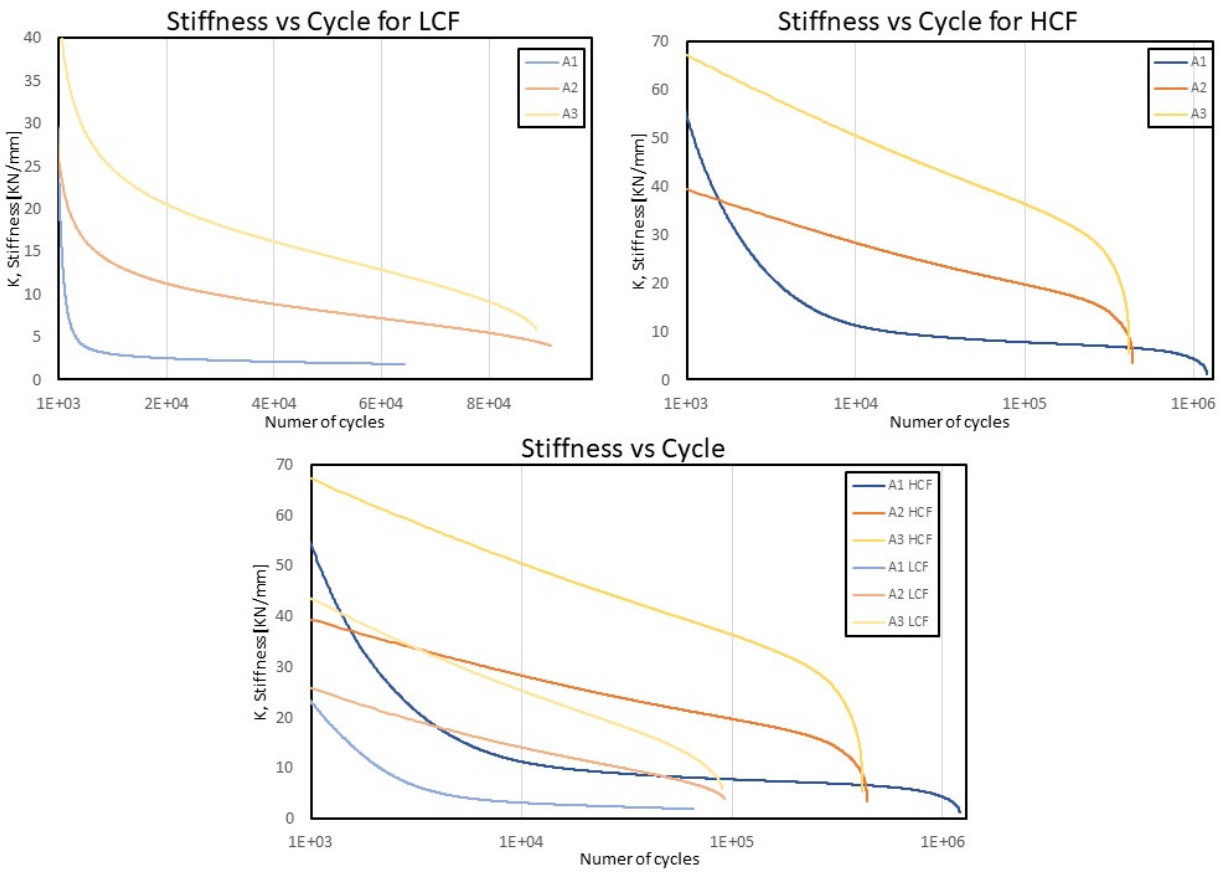

Figure 24: Stiffness vs. Cycle for low and high cycle for group A

4.3.2 Cube Size Effect with Constant Wall Thickness

For the second category, the cube size effect is investigated, meaning that for the three cube sizes of 8mm, 25mm, and 42mm, the wall thickness will remain the same at 0.625mm to consider the cube size effect exclusively. The set includes B1, A2 and B2 ordered in the magnitude of their size, starting from smallest to largest. Similarly, as in the case of the first category, where there were different cube sizes involved, the accuracy of the fabrication process diminishes asymptotically. For this reason, the actual wall thickness will deviate from the nominal value, assumably to the same extent as the variance between nominal and produced porosity, and ultimately influence how the structure behaves. With attention to the SN Curves displayed in Figure 25, there is again an outlier in set B1 containing the smallest specimens. As previously mentioned, the smaller scale will gain additional material than the intended geometry and will therefore prove stronger. However, dissimilar from A1, the relative density is even greater, which causes densification earlier in its compression range. Considering the lower regime of the SN curve for the three different sets, there are pretty significant variations between them. In the case of B1, failure occurs at 23 thousand cycles when the maximum stress peaked at roughly 290MPa. For A2 and B2, the required peak stress to reach failure at roughly 11 thousand cycles were 94MPa and 78MPa, respectively. Between B1 and A2, that is a three times difference, unlike A2 and B2, which are only separated by roughly 20 percent. By the same token, the latter stages of the fatigue life can be analyzed. Based on the regression, the fatigue limits were calculated, still showing a similar tendency. In ascending order, B1, A2, and B2 had a fatigue limit of 220MPa, 71MPa, and 61MPa. This agrees with the variation in the first part of the SN curve, as B1 is three times stronger

than A2, which again is 16 percent stronger than B2. This indicates a similar loss in integrity for the entire group in both the low and high cycle fatigue regimes. Concerning the two specimens that satisfied the runout conditions, B1 and A2 experienced this when the peak load was set to 200MPa and 68MPa, respectively. That is well within the range of the calculated fatigue limit. To summarize the behavior displayed in these plots, the SN curve shows a separation in stress between the sets, which remain constant throughout. The factors that consolidate the much better fatigue life with a smaller cube size are threefold. For one, the smaller cube sizes result in a lesser overall surface area, which cracks commonly initiate due to poor surface finish. Secondly, when kept constant, the wall thickness will become larger compared to the cube size when the size of the specimen is reduced. Lastly, and as previously pointed out, a higher relative density provides added strength which also translates to better performance under cyclic loading. Combining these factors, the effect of the cube size becomes conspicuous.

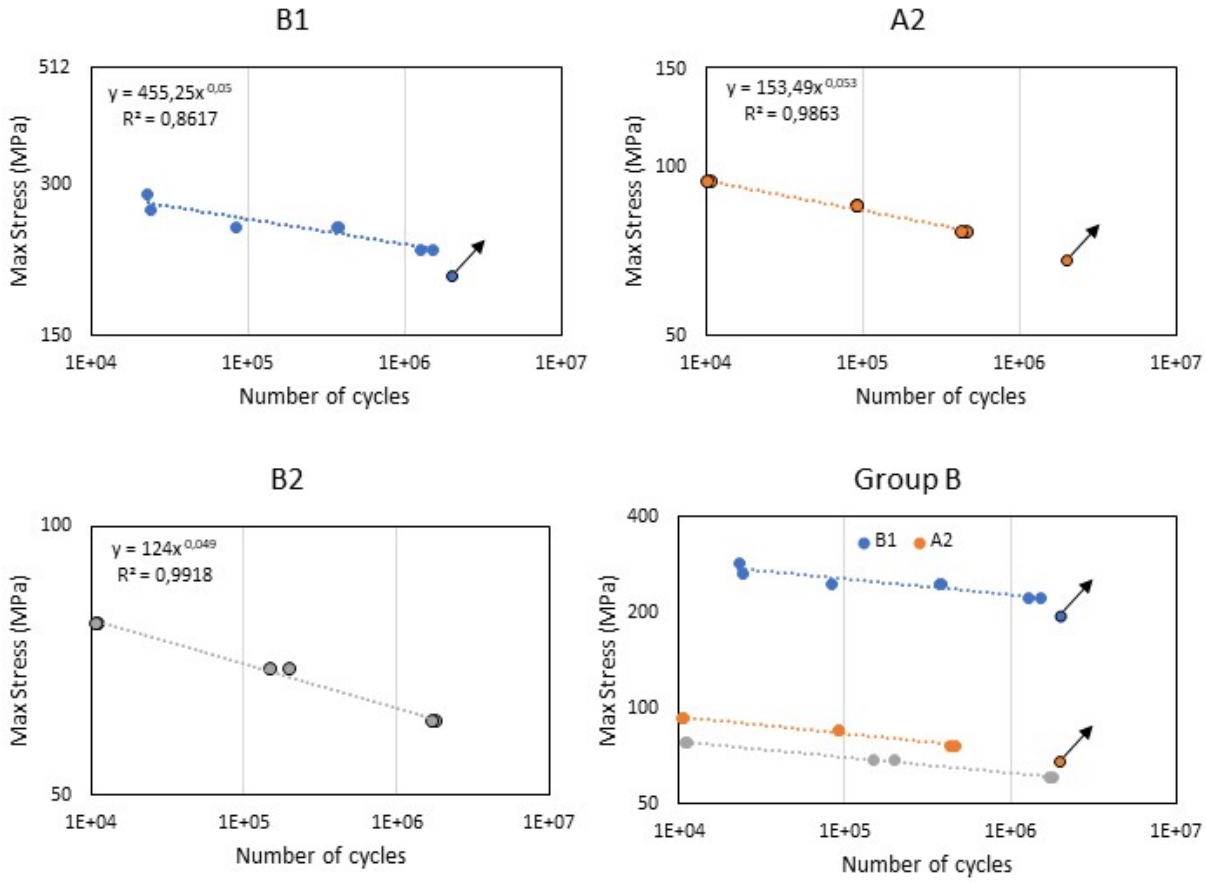

Figure 25: SN Curve - cube size effect with constant wall thickness

When normalizing based on the yield stress, the ranking between the sets is still in the same order as displayed in Figure 26. That being said, the variations have diminished substantially despite B1 remaining an aberration. In the LCF regime, A2 and B2 are quite similar in that, respectively, 92% and 87% percentage of yield results in failure. On the contrary, B1 is well above its yield strength at roughly 151% when it fails at 23 thousand cycles. In fact, B1 is in the plastic regime throughout the whole fatigue life, even in the calculated fatigue limit. Nonetheless, in the LCF regime, B1 is approximately 64 percent stronger than A2, which is 5 percent stronger than B2. In like manner, the fatigue limits exhibit more or less the same

fluctuations between the sets. Where B1 is still beyond the yield strength at 115%, A2 and B2 have a calculated fatigue limit of 69% and 68% of their yield strengths, respectively. This means that between B1 and A2, the variation is kept constant, whereas a minuscule convergence between A2 and B2 has led to a 3% difference in the fatigue limits. The most critical points of this plot can be separated into two. For one, B1 is above its yield strength in all the different stress range scenarios, indicating that densification occurs in only a small amount of cycles. By then, the structure will tolerate higher loads than the calculated yield strength, which, unlike the static test, is not based on the same compression range as the fatigue tests. In other words, the yield strength does not account for changing behavior during the compression range due to densification and strengthening of the lattice structure. Secondly, the fact that the order amongst the sets is depicted equally in the normalized and ordinary plots signifies that the effect of cube size is prominent even when accounting for the as-built characteristics such as relative density and strength. Even though the variations are minor, the effect is clearly there.

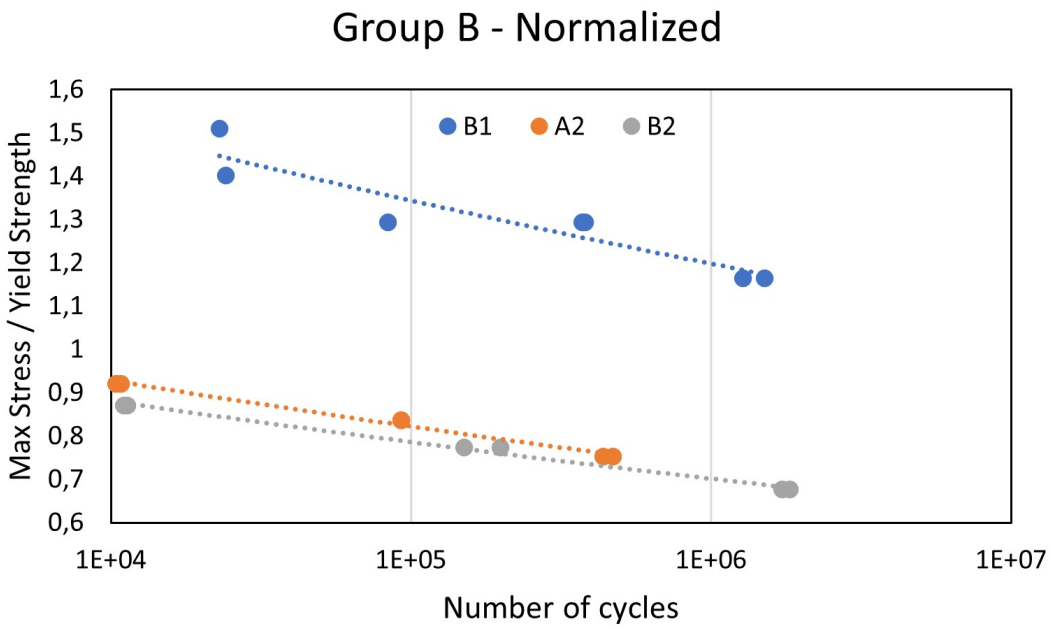

Figure 26: Normalized SN curve for group B

In the matter of the continuous loss in stiffness during cyclic loading, as illustrated in Figure 27, there are variations amongst the sets. With attention to the first of the three plots demonstrating stiffness for the LCF specimens. As the plot displays the curves from as early as 1000 cycles, it unfolds a premature and minor collapse of A2, which till then had shared its stiffness with B2. This dip is followed by a transition to cyclic softening up to the time of failure. For B2, the stiffness is more gradual throughout and shows signs of a more rapid decline at the very end. Nevertheless, the accumulated damage during the fatigue life for these two specimens is enough to ensure failure at approximately the same time. In the case of B1, the stiffness displays little change throughout the fatigue life and, as such, becomes stiffer than A2 and B2 at roughly 4200 and 5800 cycles, respectively. Much like before, none of the LCF specimens show a rapid decline in the latter stages of their fatigue life. Even more so in the case of B1, where the densification provided more stiffness and a more gradual approach to the boundary condition of 20% displacement. Moving on to the stiffness presented in the HCF plot. Unlike the former plot, A2 does not collapse in the beginning stages of the fatigue life now that the force has been reduced. This also means that amongst A2 and B2, the progressive loss in stiffness follows a close path. What can be said about the latter stages for these two sets is that right

before they encounter the most rapid decline in stiffness as a response to fractures in the structure, there is a segment of a slight decrease in the rate of continual stiffness loss. After all, some sort of compacting of the internal geometry will occur and ultimately reduce the rate of change in stiffness. When it comes to B1, the rate of stiffness loss remains more or less the same as before. There are still no indications of a rapid decline in the closing stages, which, interestingly enough, was something A1 experienced despite the similarities in porosity. As known, B1 is more compact, suggesting that densification progressed more rapidly, leaving no struts or otherwise porous geometry inside the structure.

In the final plot that combines the test for low and high cycle fatigue, there is an obvious likeness in the stiffness rate between each set. Moreover, where B1 shows a higher stiffness in the case of the LCF specimen, both the HCF specimens for A2 and B2 maintain a higher stiffness. In summary, there are undoubtedly similarities between group B and the previously reviewed group A. Recognizing that they both have aspects of the cube size effect that inherently makes for denser structures, the stiffness in group B fits the same narrative as before: A more retained stiffness loss for the smallest cube size and an increasingly higher and more rapid loss in stiffness for the more porous structures. Having said that, between A2 and B2, which holds the two larger cube sizes of 25mm and 42mm, the deviation is inferior as opposed to what was observed for A2 and A3. Besides this, A2 is the stiffest lattice in this group, unlike group A, which displays A3 as the stiffest lattice. Although their sizes can be one element in comparing the two groups, porosity is not the same and is arguably the reason for the variations between the groups in what portrays the stiffest lattice in each.

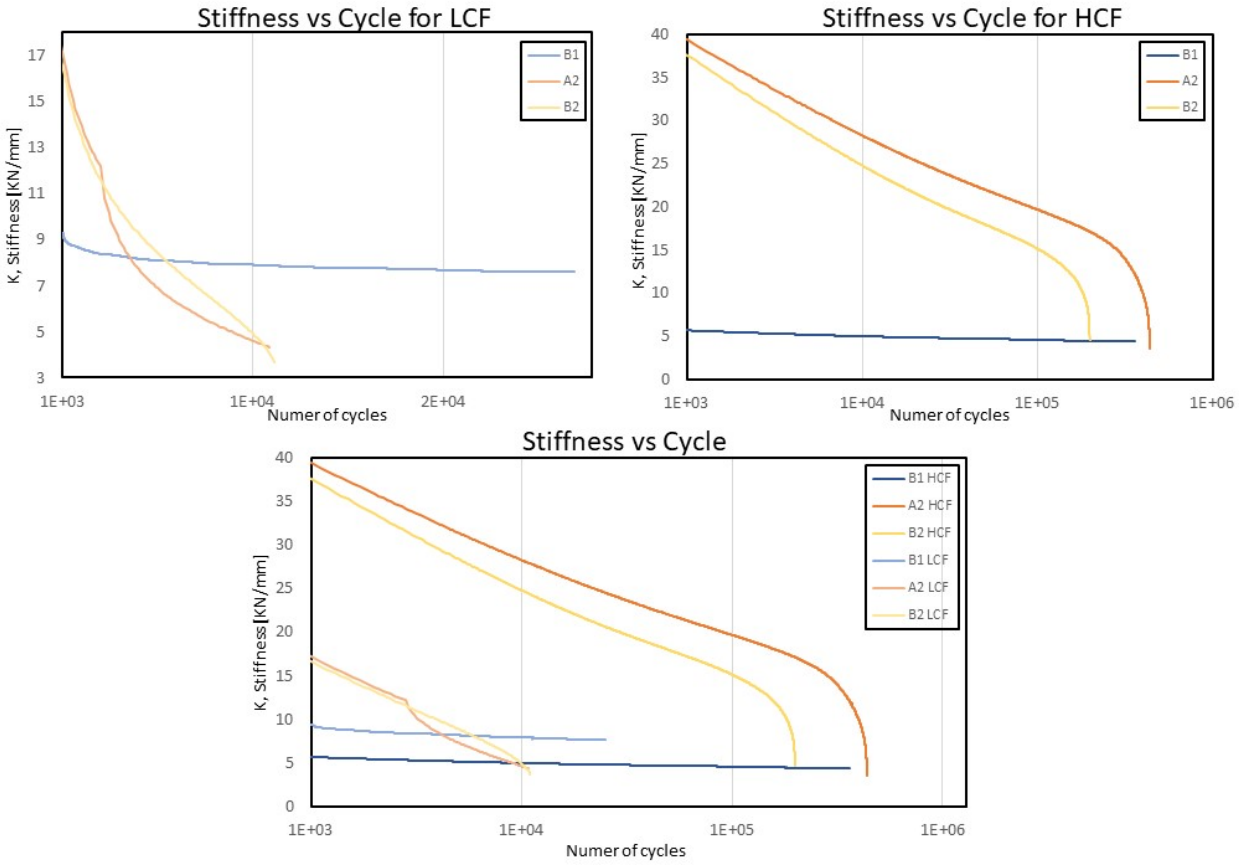

Figure 27: Stiffness vs. Cycle for low and high cycle for group B

4.3.3 Wall Thickness Effect with Constant Cubic Size

For the last set, C1, A2 and C2 are examined where the wall thickness is the varying factor between them with a constant cube size of 25mm. As previously mentioned in section 3, C1, A2, and C2 specimens have a wall thickness of 0.2mm, 0.625mm, and 1.05mm, respectively. Starting with the most apparent difference between them with respect to the SN plots in Figure 28, the thicker specimen C2 seems to be superior in terms of fatigue strength in the low cycle fatigue regime. For instance, when considering the stress at roughly 10 thousand cycles till failure, the stress is 62MPa, 95MPa, and 141MPa for C1, A2, and C2, granted that the pair C1 and C2 are calculated based on regression, whereas A2 was a test that failed in the proximity of 2 million cycles. This is likely because roughness does not scale with the wall thickness, which means that for a thinner specimen, the preexisting cracks and notches are more significant to the wall thickness; hence, less crack propagation is required for the thinner specimen to reach failure. However, when looking at the HCF regime, the difference seems to diminish gradually, and eventually, the three sets are approaching the same stress and cycles required for failure. The regression states a fatigue limit of 50MPa for C1, 71MPa for A2, and 80MPa for C2, which is considerably closer than the LCF regime. Correspondingly, the runouts for C1 and A2 match these values where the former tests achieved runout at the same load as the calculated fatigue limit, and A2 reached run out status when loaded with 68MPa. This convergence is presumably caused by the different failure mechanics operating for low and high stresses. As previously mentioned in section 2.3, a lower stress state will mean that most of the fatigue life promotes the development of new cracks. On the other hand, the fatigue life in a high-stress state will primarily propagate preexisting cracks, which means the roughness compared to the wall thickness will play a larger role in this state. In other words, the roughness in relation to the thickness will be more consequential when the stress is higher, but as seen in the SN plot, it will decrease its efficacy as the stress is lowered. Since only one specimen for C1 and C2 was tested at this stress level, there is a possibility that these could be outliers. However, based on the strong convergence trend in the SN curve combined with the calculated regression, this effect seems quite compelling. There is also a point to be made in that a larger wall thickness will simultaneously increase the surface area, which introduces more imperfections. Despite this, the relation between the sets makes it clear that the larger wall thickness seems to be the dominant factor.

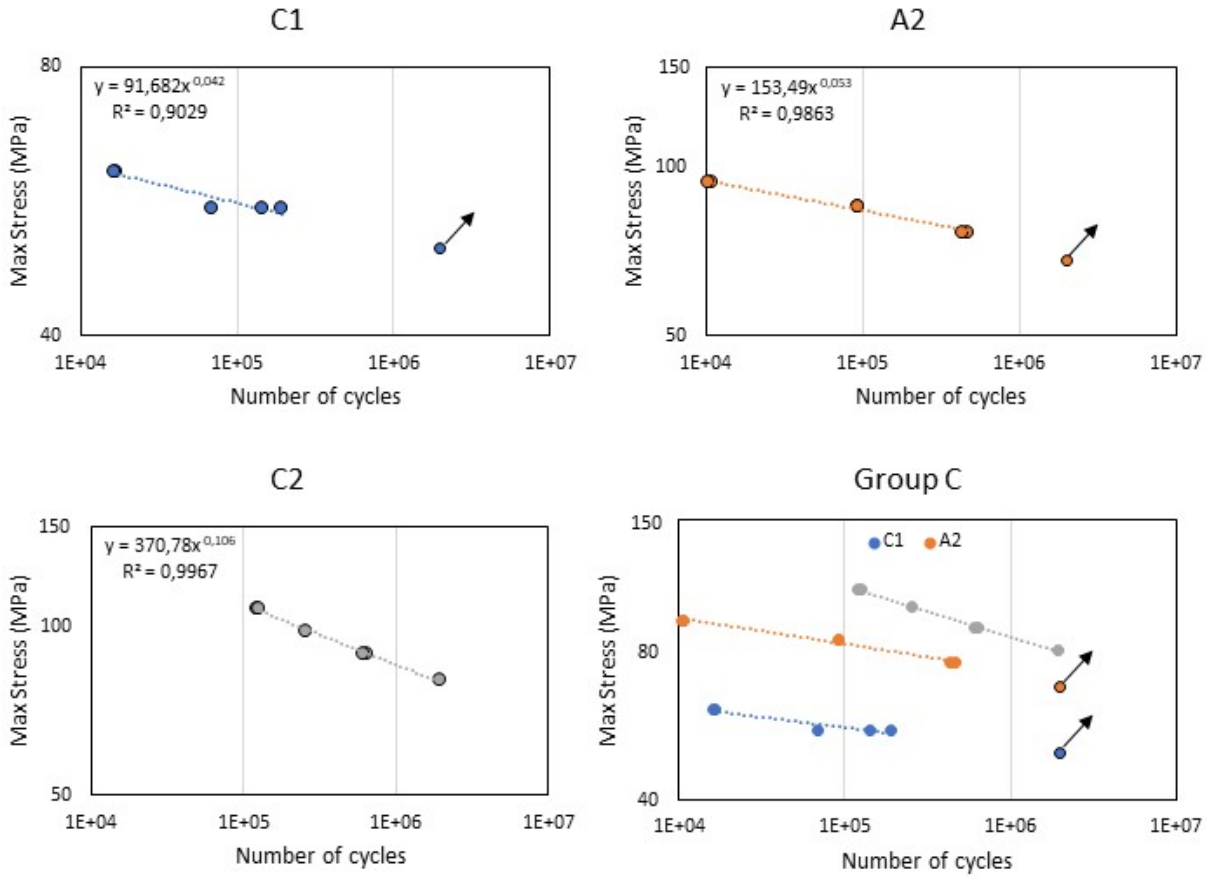

Figure 28: SN Curve - wall thickness effect with constant unit cell size

In the case of the fatigue plot normalized on the yield strength, as seen in Figure 29, the hierarchy changes, and an even closer convergence is observed when reaching the fatigue limit. In the same notion as before, the low cycle fatigue shows failure at 10 thousand cycles when loading C1, A2, and C2 with 85%, 93%, and 112% of yield, respectively. However, as the stress levels are reduced, C2 crosses both A2 and C1, which ultimately results in C2 having the lowest fatigue limit, 63% of yield. For C1, the fatigue limit is 68% of yield and 69% of yield for A2. What seems to be the overall trend when accounting for the yield stress is an even larger difference in how these three structures behave between the low and high cycle fatigue regimes. Inherently, a normalization based on the yield strength should, in principle, remove the effect of added strength due to a larger cross-section. What is still prominent after normalization is the effect of surface area. Unlike the first SN curves, the surface area becomes a dominant factor, which could be why C2 has such a detrimental loss in integrity in the HCF regime compared to C1 and A2. A similar action can be seen in A2 as also this set has a larger steepness to its curve than C1. Conversely, A2 is still providing a slightly higher fatigued limit than C1, although this may just be a case of small inaccuracies in the calculated yield strength or just the nature of how the geometry handles higher loads which changes where the two regression curves intersect. In general, this means that the most desirable geometry will change at certain stress levels and wall thicknesses. For instance, if a structure were designed to last for approximately 100 000 cycles, C2 would be preferred. On the other hand, designing a structure for more than 1 million cycles would prove the first statement false as now A2 would be the best option. Nevertheless, as previously mentioned, the effect of the larger wall thickness is still true for the low cycle fatigue regime. However, the effect of the surface area seems to be

more influential in the high cycle fatigue regime seeing that the weakest set of the three is C2.

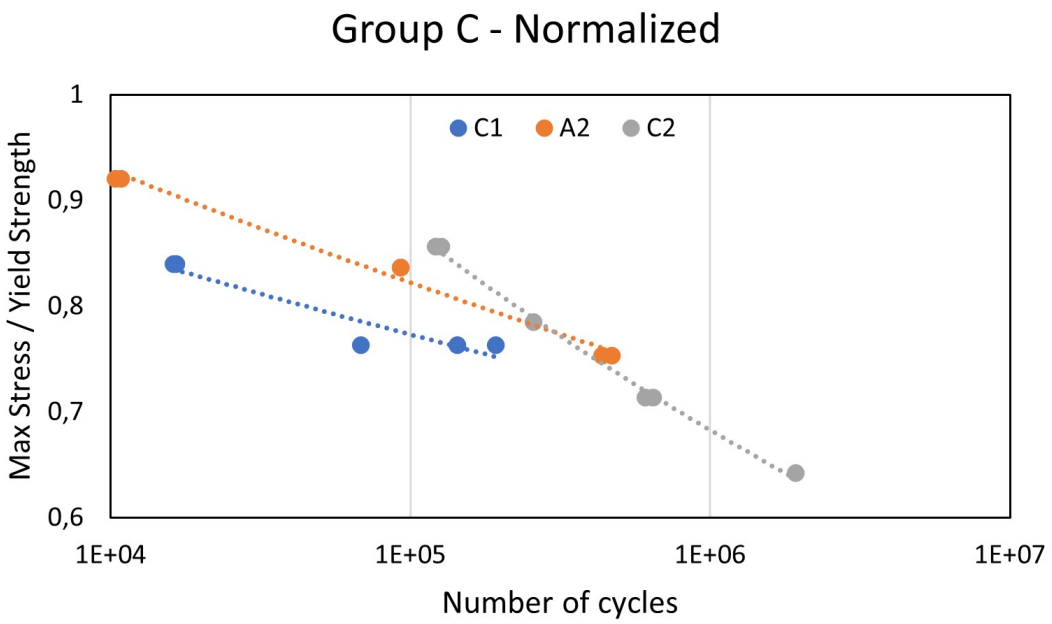

Figure 29: Normalized SN curve for group C

Lastly, there are also the stiffness plots for group C that illustrate the compliancy of each specimen throughout the fatigue life as seen in Figure 30. When considering the first of these plots being for the low cycle fatigue, the initial magnitude of stiffness seems to be in the same order as the relative density of the three specimens. In other words, a higher stiffness is found as the relative density increases. However, there are some variations in the number of cycles till failure, especially between A2 and the pair of C1 and C2, which means that the rankings in stiffness do not stay the same throughout the entire fatigue life. What also seems different is the amount of rapid loss in stiffness when approaching failure. Here the trend seems to be that a higher porosity makes for a more rapid loss, whereas the opposite can be said for specimens with lower porosity. This again corresponds to what has been previously found for the two other groups. Apart from these differences and that C1 has a slightly lower rate of loss in stiffness, the behavior appears to be quite similar amongst the sets. For the high cycle fatigue, it is apparent that the stiffness remains higher during the fatigue life compared to the low cycle fatigue as a consequence of a lower force that produces a smaller displacement. Still, some of the previously discussed trends from the low cycle fatigue persist in high cycle fatigue. For one, the stiffness is still based on the relative density of the specimens. Moreover, C1 still seems to have a slower rate of stiffness loss, whereas A2 and C2 are more or less identical. Still, C1, although close to failure, was runout and could have experienced a similar loss in stiffness if a failure occurred prior to the runout limit. In the latter stages of the HCF plot, there is now a prominent decline in stiffness for A2 and C2. Much like the case for sets A2 and B2 in group B, there is a slight decrease in the rate of stiffness loss right before the structure encounters fracture and subsequently loses integrity. The last plot combining them all is more of the same story. On all accounts, the specimens in the high cycle fatigue regime provide a higher stiffness than those in the low cycle fatigue regime. In short, these plots indicate that a larger wall thickness aids in stiffness but consequently has a higher rate of stiffness loss during the fatigue life until failure occurs. The higher relative density also provides a more gradual approach to failure in the LCF. The required displacement is met mostly due to plastic deformation rather than cracks large enough to cause fractures. The latter is the case for C1 in the LCF regime.

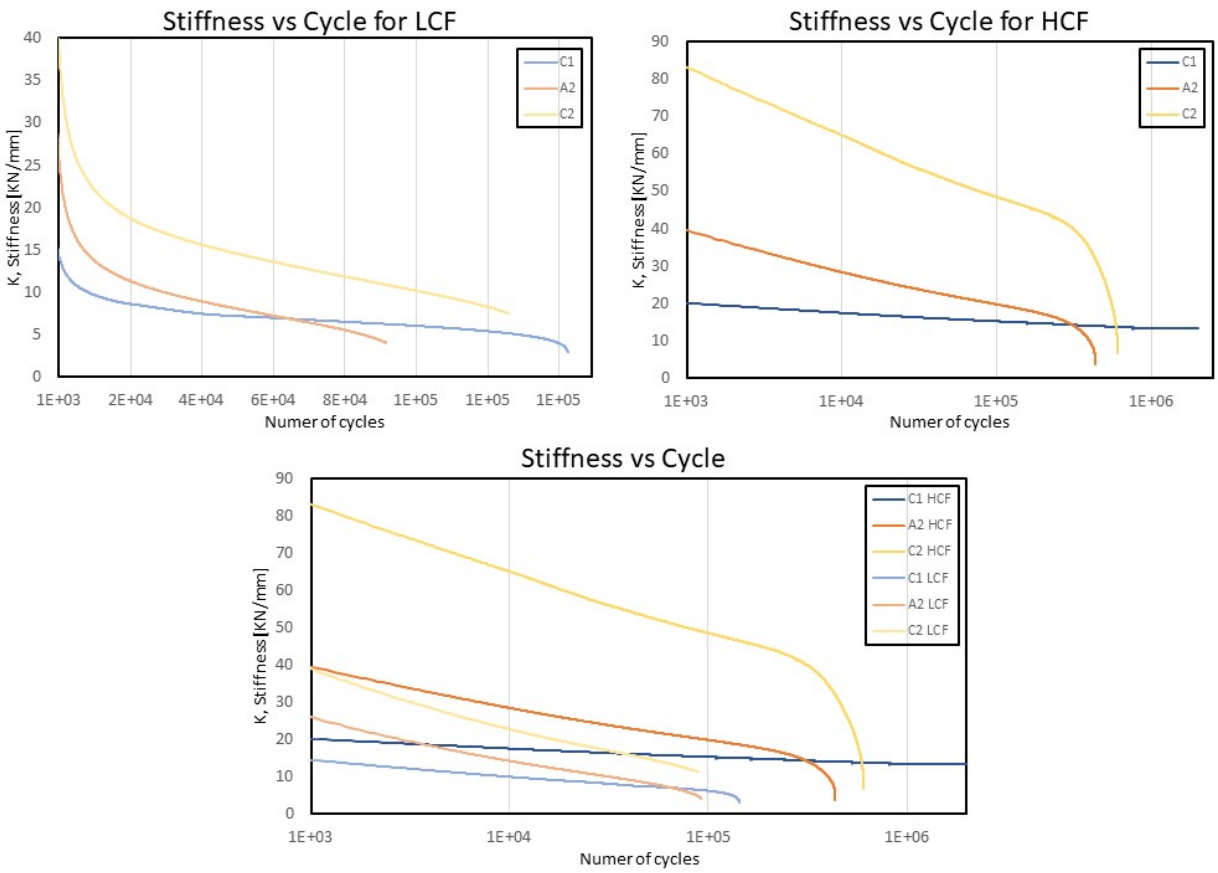

Figure 30: Stiffness vs. Cycle for low and high cycle for group C

4.3.4 Short Overview and Evaluation of All Sets

For a complete overview of the fatigue data, an SN plot and a normalized SN plot for all the various sets can be seen respectively in Figure 31 and 32. In terms of the former plot, the most noticeable trend is that, on all accounts, the fatigue strength of the lattice corresponds directly to the relative density. Put differently, the order observed in the SN plot is the same as the relative density in both LCF and HCF. More interestingly is the latter plot, as this illuminates the fatigue strength without the influence of individual strength. Apart from B1, which remains an outlier because of excessive densification within the displacement limits of the fatigue tests, the progression between the rest is clear. From high variations amongst the sets in the low cycle fatigue regime, a convergence presents itself in the high cycle fatigue regime. Additionally, the rankings, which still was determined by the relative densities, also changed when approaching the fatigue limit. Under those circumstances, the effect of relative density goes from being quite significant in LCF to being a minor part of HCF in determining the fatigue strength. Inversely, the effect of roughness, surface imperfections, and the surface area seems to gradually be the more dominant factor in the later stages of fatigue life. All of which have previously been discussed between section 4.3.1 and 4.3.3. Moreover, in Table 10 and Figure 33, the fatigue limits are presented in both fashions, one for peak stress during full compression and the other as a ratio based on the respective yield strengths. To begin, B1 still shows a uniquely large fatigue limit but simultaneously is well above its yield strength at 115%. It is arguably not a result defined by its porous structure but rather the premature densification of one. Unlike B1, the rest of the sets are inside the bonds of the yield strength, more precisely ranging from 63% to 75%. Incidentally, the relative density does not seem to dictate the rankings now that A3 displays the highest percentage of yield and C2 the lowest. Between the four reaming sets, the percentage of yield that meets the fatigue limit requirements spreads only 2%, ranging from 68% to 70%.

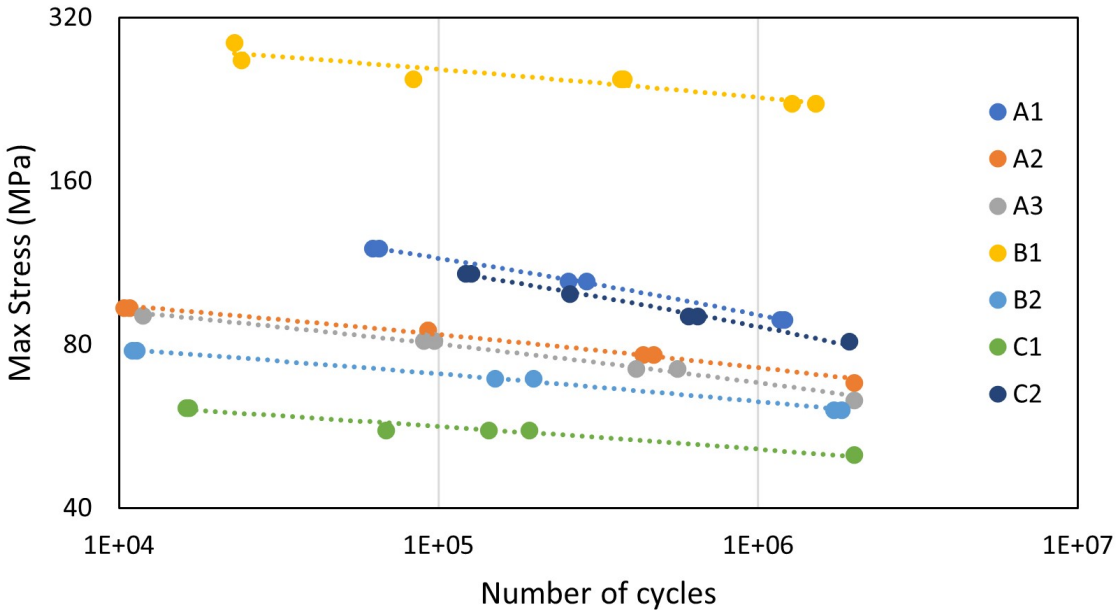

Figure 31: SN Curves for all sets

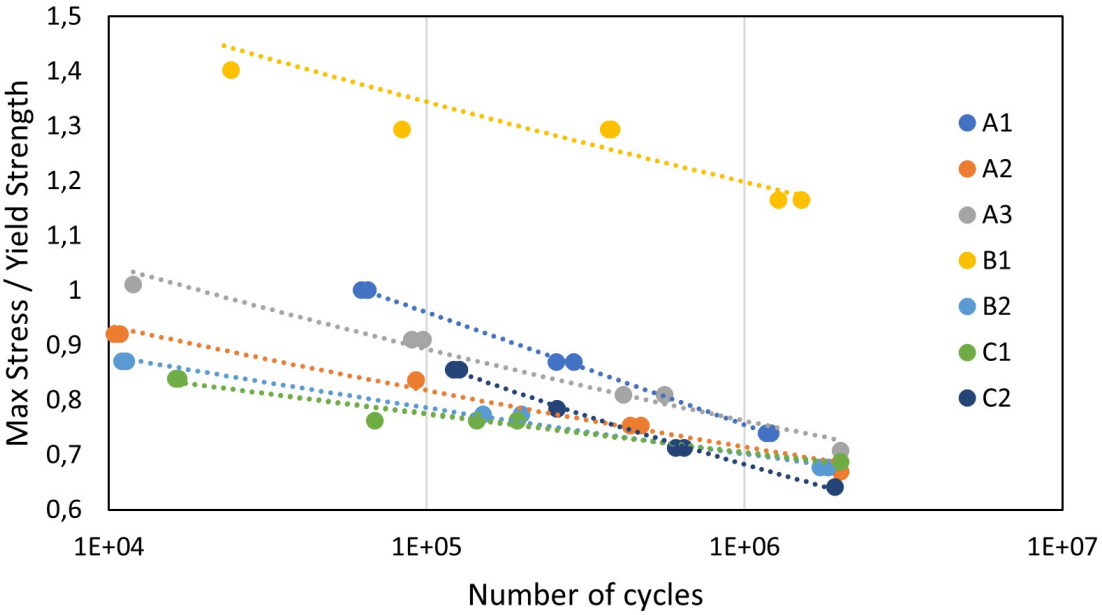

Figure 32: Normalized SN Curves for all sets

Table 10: Fatigue Limits

	A1	**A2**	**A3**	**B1**	**B2**	**C1**	**C2**
Fatigue Limit [MPa]	85	71	67	220	61	50	80
Fatigue Limit / Yield Strength	0.70	0.69	0.75	1.15	0.68	0.68	0.63

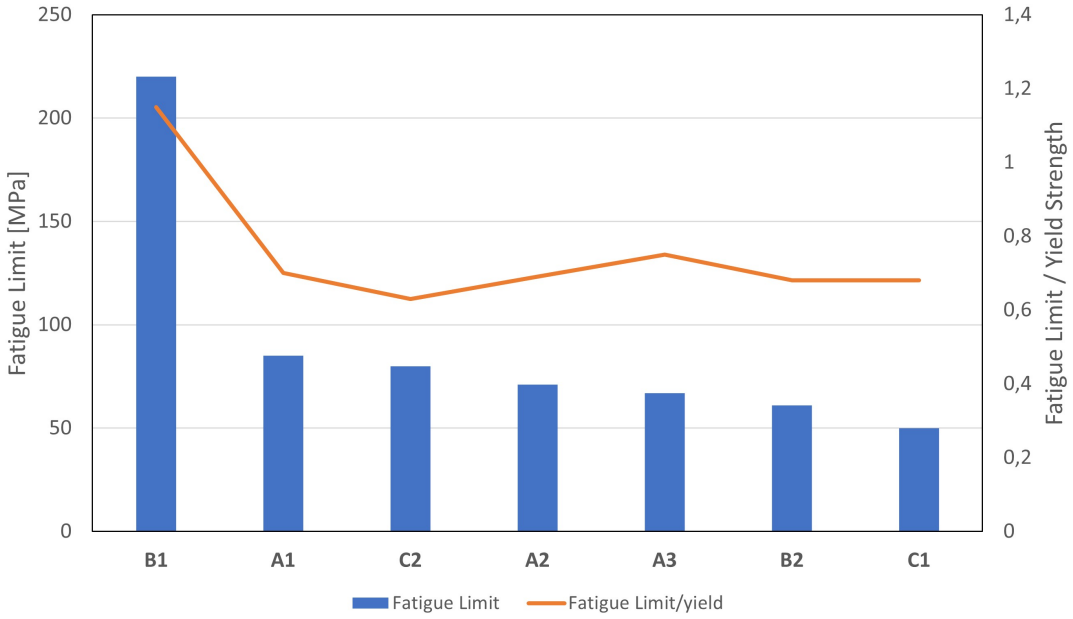

Figure 33: Fatigue Limits for all the sets

4.4 Failure Mechanisms

In this section, high magnification images obtained by digital microscopy and SEM explain global and local fracture locations from fatigue testing and provide insight into the surface topology. The surface examined is the same for each specimen, one of the side surfaces to the build and loading direction. For each individual set, both a low cycle and high cycle fatigue failure were considered to see how different stress amplitudes affect the extent of the fractures. In an effort to make the results as comparable as possible, a similar number of cycles for both the low and high cycle fatigue cases were chosen between the sets. Additionally, some of the run-out specimens are also examined at the very end of the section. The elected specimens can be seen in Table 11 and 12, where the test number, stress, and the number of cycles to reach failure is denoted. Furthermore, the illustrations are categorized in the same groups as before and can be seen in alphabetic order from Figure 34 through 36, with the runouts displayed in Figure 37.

Table 11: Elected Specimen for Analysis

Set	Test No.	Peak Stress [MPa]	Cycles till Failure
A1	7	120	65 164
	8	89	1 210 226
A2	6	94	10 378
	1	77	470 445
A3	3	90	11 914
	2	72	559 690
B1	9	288	23 031
	8	222	1 511 007
B2	3	78	11 345
	2	61	1 825 670
C1	8	61	16 223
	4	55	192 562
C2	2	108	121 439
	4	82	1 924 041

Table 12: Fatigue with Number of Cycles Achieving or in Vicinity of Runout Condition

Set	Test No.	Peak Stress [MPa]	Cycles till Failure	Cycles through Regression
A2	7	68	2 000 000	4 669 970
A3	5	63	2 000 000	4 773 764
B2	2	61	1 825 670	2 236 458
C1	2	50	2 000 000	1 793 300
C2	4	82	1 924 041	1 862 373

First and foremost, it is quite evident that there are similarities in local failure locations and the direction of crack propagation between all the specimens that have been tested. The most exposed locations for these cracks are in the top and bottom parts of the sinuous geometry, of which there are likely two factors at play. For one, these are the locations with the highest stress concentrations, which makes these locations most prone to fatigue failure, as further discussed by Abueidda et al. [1]. Secondly, and much of the reason for these stress concentrations in the first place, these locations are the most susceptible to forming excessive metal particles during the fabrication process, often referred to as overhangs. In forming small pockets of metal particles beneath the sinuous geometry, it will effectively be hot spots for small cracks and otherwise sharp edges, a probable location for cracks to develop further. From the close-up figures of these crack locations, the crack appears to propagate upwards due to the high stresses around the crack tip. In the same

fashion, the cracks that initiated from the lower sections of the sinuous geometry propagated downwards. Another expected behavior that encompasses all the sets is the difference in the number of cracks formed between a low and high cycle test. This again can be traced back to what was previously stated in Section 2.3. A low cycle test is exposed to more plastic deformation and, as such, leads to a more rapid deformation of the lattice, resulting in a fewer number of cracks required to achieve failure. On the other hand, a high cycle test will, after a short while, reach a steady-state with a minor rate of deformation. This leaves more time for small cracks to propagate and grow larger. Therefore, high cycle fatigue failures are often a result of complete loss in integrity of the structures because too many cracks have formed, resulting in global fractures. For several of the high cycle tests, the global fractures develop diagonally to the side surface, although the extent of this seems to be governed by the relative density of the structures.

In Figure 34 which showcases tests from group A, both A2 and A3 show similar failures in the HCF regime with global fractures along its side surface. Besides this, the contrast between low and high cycle fatigue is drastic when comparing the scale and the number of cracks. On the other hand, A1 is more similar between the two regimes, although the cracks are slightly larger and more abundant in the case of HCF. Regardless, the degree of global fractures is not prominent to the same degree as the other pair, likely due to the increase in relative density. With attention to the surface topology, the roughness is substantially worse for A1. For A2 and A3, it becomes increasingly better, even more so when considering the roughness in relation to the feature's thicknesses, which to a large degree dictates the amount of propagation required for initial cracks to become local fractures in the geometry. Moving on to group B, illustrated in Figure 35. Here, many of the same differences displayed in group A that presented themselves due to variation in relative density remain the same. Specifically, the size and amount of cracks between the low and high cycle tests for B1 are almost identical to B2, which shows a significant change, not to mention the typical global diagonal failure for these HCF specimens. But unlike previous discoveries, B1 display only a fraction of the cracks that comparably A1 display. In identifying that B1 is more or less solid, leaving little to no room for deformation in the structure, especially in places with an abundance of imperfection, there is an absence of the tensile stresses that normally open up the cracks. Instead, most of the fatigue life is a gradual plastic deformation of the entirety of the structure. Aside from this, the surface topology will again be influenced by the cube size of the specimen. However, since B1 has such a large wall thickness compared to its size, the surface roughness might not be particularly influential, especially when considering the lack of cracks. Nevertheless, B2 shows a much finer relation between the roughness and the thickness of its features. The last of the groups is group C which can be seen in Figure 36. For the low cycle fatigue specimens, C1 displays small amounts of propagation of the visible cracks compared to C2, although there is some discrepancy in the number of cycles till failure for the two. Similar to groups A and B is what occurs in the HCF regime. Apart from the increase in size and amount of cracks, there is again a difference in failure mechanics between the low and high relative density specimens. Where C1 shows the same global fracture as before, C2 shows a more composed final form despite the fact that there is a multitude of cracks. The cube size of these lattices is the same, as well as the surface roughness and imperfections. However, these two factors prove more detrimental in the case of C1 due to the thinner structure it provides, resulting in a much higher ratio between the roughness and the size of its features. Finally are the specimens in figure 37 that achieved runout or were in the vicinity of the boundary condition. A2, A3, and C1 were the tests that achieved runout but still showed significant amounts of crack and several locations with merging cracks. The two former specimens are far from the calculated cycles to reach failure. Therefore, they are a good indication of how most imperfections form into cracks, not to mention the behavior during the initial propagation. On the other hand, both B2 and C2 describe how the cracks look when they have reached a critical point. Furthermore, C1 is the only runout specimen that outperformed the cycles calculated with regression, although rapid fractures and failure were likely not far from happening. Inversely, B2 was calculated to go beyond the runout limit and yet failed in advance. Seeing that this specimen experienced a global fracture, it may have been a premature failure where coincidentally, most of the propagated crack intersected and led to a large enough fracture to force the lattice to compress and reach the displacement limit. C2, however, did not display any global fractures and proceeded to last for more cycles than the regression enforced.

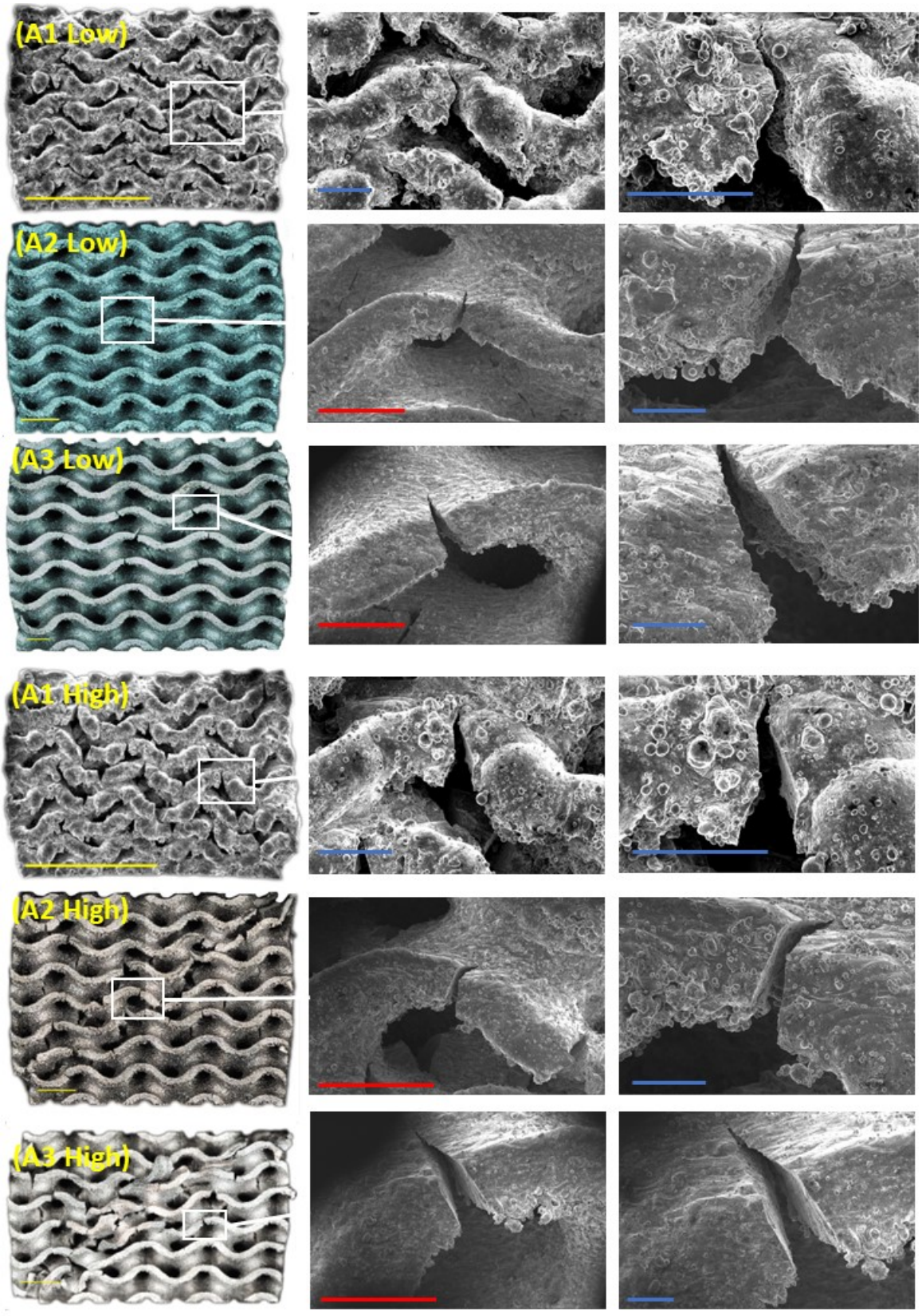

Figure 34: Low and high cycle fatigue group A (scale-bar yellow, red and blue: 4mm, 2mm and 500μm)

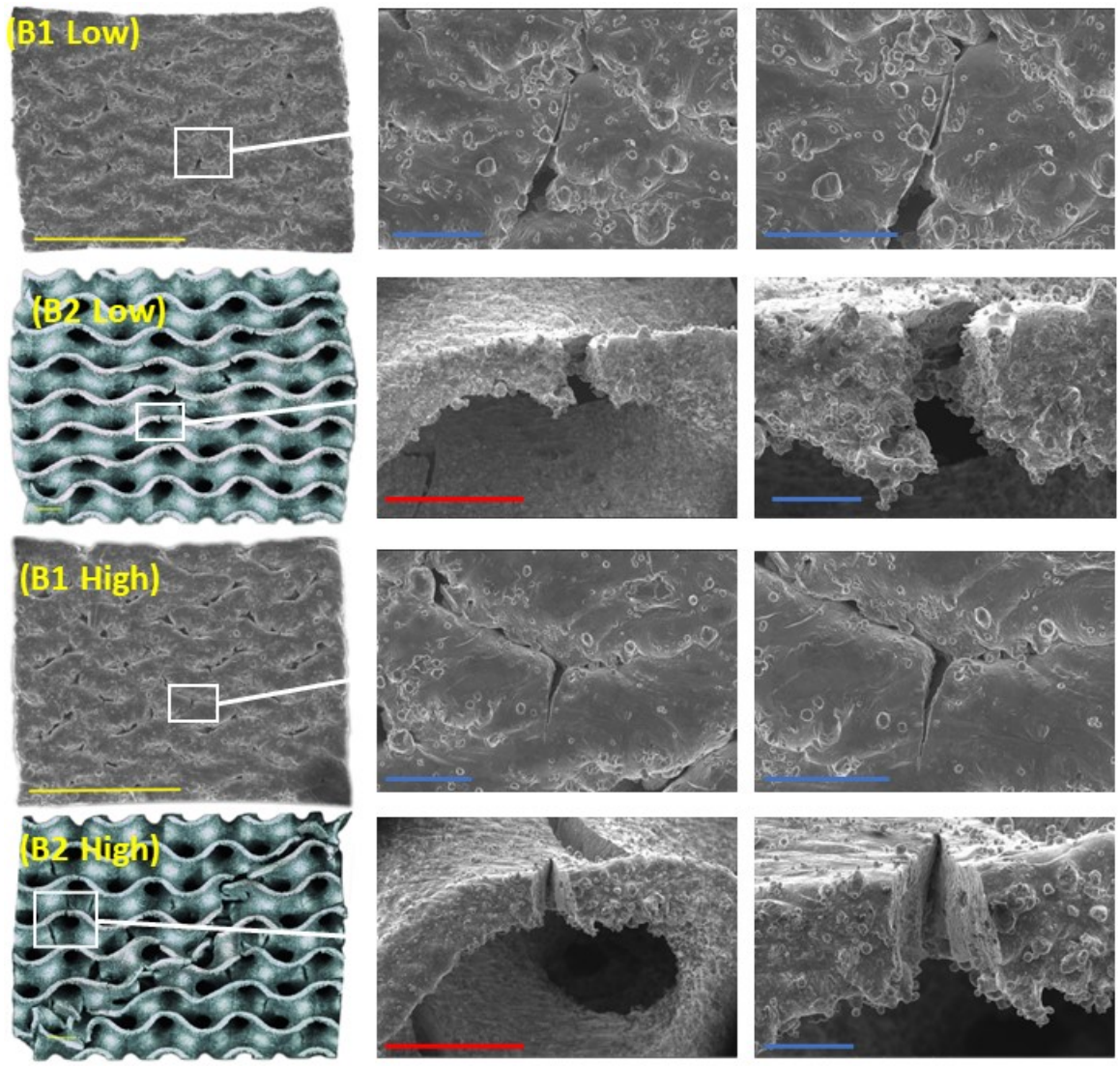

Figure 35: Low and high cycle fatigue group B (scale-bar yellow, red and blue: 4mm, 2mm and 500μm)

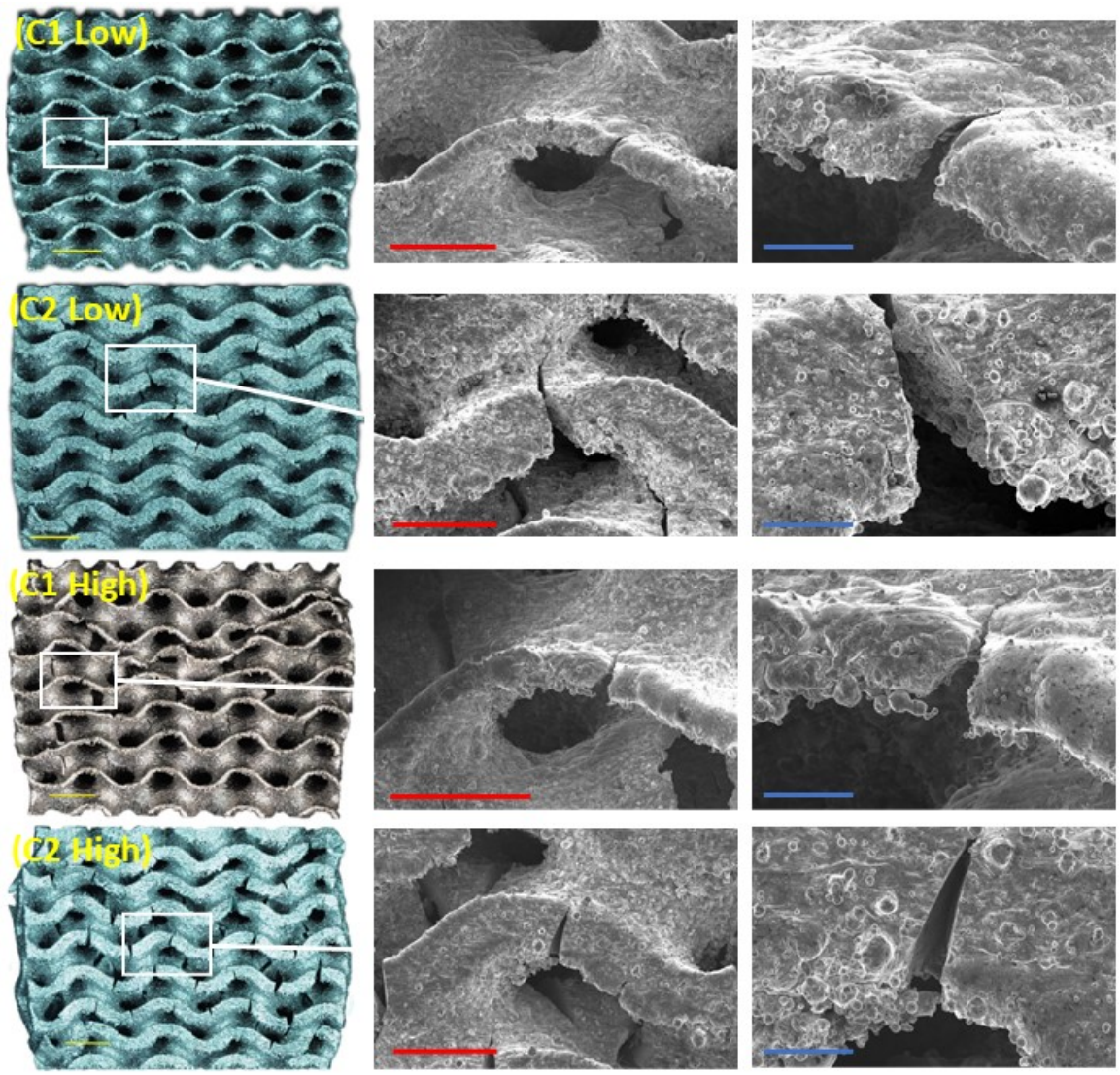

Figure 36: Low and high cycle fatigue group C (scale-bar yellow, red and blue: 4mm, 2mm and 500μm)

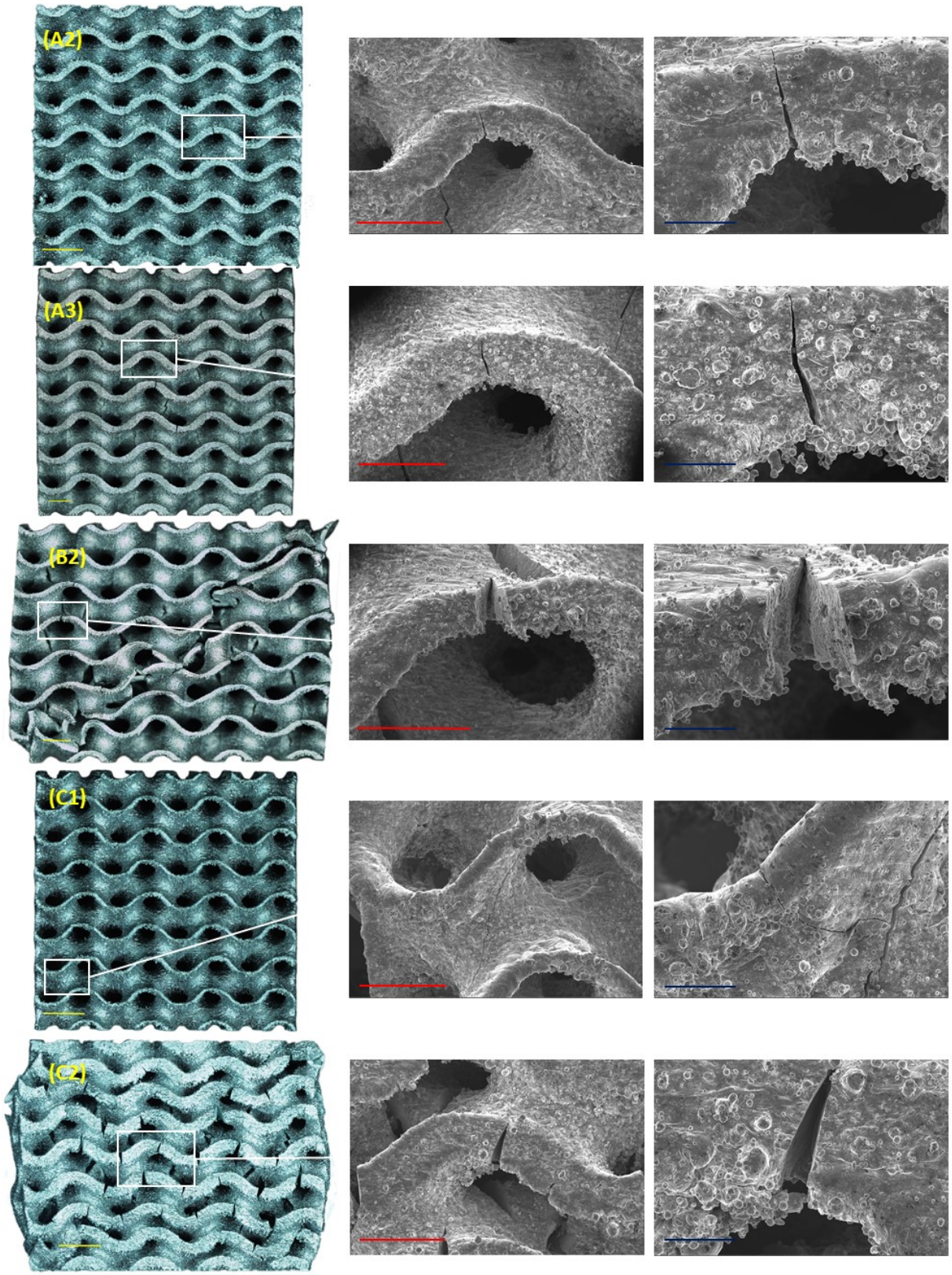

Figure 37: Runout fatigue cracks (scale-bar yellow, red and dark blue: 4mm, 2mm and 500μm)

5 Conclusion and Further Research

In this master thesis, the research aim was to study the effects of scale, size, and wall thickness concerning mechanical and fatigue properties of AlSi10Mg sheet-based gyroid lattice structures fabricated through additive manufacturing. Besides these studies, CT scanning was also utilized to investigate variations between the actual and modeled geometry and SEM for close-up imagery to investigate the failure locations formed during the fatigue testing. Through these analyses, there were many interesting findings. First, the CT scanning provides a clear relationship between the cube size of a specimen and the deviation from the intended geometry. In other words, larger cube sizes proved superior to the smallest cube size, which gained excessive material in comparison. Secondly, the static compression tests displayed a few different behaviors. In general, a more porous structure is more susceptible to sequential collapses, whereas the denser structures have a gradual stress plateau except for B1, which solidified at a premature strain. In addition, the calculated yield strength demonstrated that strength increased proportionally to the volume fraction, which is in agreement with the discovery of Yan et al. [33]. Thirdly and most importantly is the analysis of the fatigue behavior. For group A which explored the scale effect, the capacity against fatigue favors smaller scales, particularly in the LCF regime, as there is a slight convergence amongst A1 and the other sets when approaching the fatigue limit. When comparing the ratio between the applied stress and the yield strength, the HCF regime confirmed the opposite as the largest scale proved best, with the two smaller scales providing a lower but similar fatigue limit. Still, it is A1 that provided the highest stress compared to its yield strength in the LCF regime. The variations between these two regimes indicate that failure in the HCF regime is governed by the relation between surface imperfections and the size of features. Hence, the largest scale displayed a higher fatigue limit compared to yield strength. In terms of the cube size effect in group B, the effect on the fatigue strength is conspicuous in that a smaller cube size proved superior, much like that of group A. In short, a smaller cube size results in less surface area; a larger wall thickness in comparison to the size of the specimen, not to mention added strength with a higher relative density. When normalized, the ranking remained the same in low and high cycle fatigue, although the effect of cube size is minor. Hence, when cube size varies, the relationship between fatigue and yield strength correlates. As of B1, the stress is well above the yield strength throughout, reinforcing premature densification due to unintended excessive material. For group C, which has equivalent cube sizes but varying wall thicknesses, the results demonstrated a steady increase in fatigue strength when increasing the wall thickness. The same can be said in the LCF regime when the yield strength is accounted for. However, the HCF regime displays a lower fatigue limit for C2 and a minor difference between C1 and A2. The varying steepness that causes these differences is attributable to the wall thickness effect. In the LCF regime, increased stiffness provided by a thick structure can withstand higher loads. On the other hand, in the HCF regime, the added surface area includes more imperfections, leading to more cracks forming and subsequently a premature failure. Concerning the compliance of the lattice throughout the fatigue life in the instance of LCF and HCF, the notion is that a denser lattice loses stiffness more gradually. In contrast, a high porosity lattice is more prone to a rapid loss in stiffness. Regardless, on all accounts, a larger scale provided higher stiffness. Lastly, the SEM imagery displayed exposed locations for cracks to develop along the top and bottom parts of the sinuous geometry. The most critical crack is formed here because of the poor surface finish in overhang regions such as these, coupled with the fact that these are also the locations with the highest stress concentrations, as further discussed by Abueidda et al. [1]. Additionally, the fracture mechanics vary depending on the thickness of the features and if the lattice is exposed to high or low loads. In short, a thin-walled specimen will, under high loads, have global fractures, but if the relative density is above roughly 50 percent, the structure remains more intact.

The accumulated findings suggest several relationships amongst the different groups and provide insightful information on the fabrication aspect and failure mechanics. However, the findings of the fatigue properties are subject to large deviations between the intended and actual parameters that define the three groups. As such, it is hard to pick out the significance of the theoretical effects as opposed to how much the inaccuracies of the fabrication process dictated the fatigue strength. Based on these conclusions, some methods can be enforced to ensure that nominal and actual geometry is similar. Firstly, the smallest groups of specimens should have a larger unit size to minimize defects and other unwanted problems that come with too small

features. Instead, the three-unit sizes could have been set to 25mm, 42mm, and 60mm, for instance, which would provide smaller differences in fabrication accuracy between them. Just reviewing Figure 14, it again shows how much more similar the accuracy is between cube sizes of 25mm and 42mm in comparison to the specimens with a cube size of 8mm. Secondly, iterative fabrication of the specimens could assist in lattices closer to the intended geometry by carefully adjusting the CAD file parameters for manufacturing. This iterative process would include smaller features than intended at locations where excessive material forms typically, and by the end of each iteration, measurements from CT scanning can provide an insight into whether or not the CAD file needs further adjustments.

Bibliography

[1] Diab W. Abueidda, Mohamed Elhebeary, Cheng-Shen (Andrew) Shiang, Siyuan Pang, Rashid K. Abu Al-Rub, and Iwona M. Jasiuk. "Mechanical properties of 3D printed polymeric Gyroid cellular structures: Experimental and finite element study". In: *Materials Design* 165 (2019), p. 107597. ISSN: 0264-1275. DOI: https://doi.org/10.1016/j.matdes.2019.107597. URL: https://www.sciencedirect.com/science/article/pii/S0264127519300176.

[2] M.F Ashby. "The properties of foams and lattices". In: *Philosophical Transactions of the Royal Society A: Mathematical, Physical and Engineering Sciences* 364.1838 (2006), pp. 15–30. DOI: 10.1098/rsta.2005.1678. eprint: https://royalsocietypublishing.org/doi/pdf/10.1098/rsta.2005.1678. URL: https://royalsocietypublishing.org/doi/abs/10.1098/rsta.2005.1678.

[3] M. Benedetti, A. du Plessis, R.O. Ritchie, M. Dallago, S.M.J. Razavi, and F. Berto. "Architected cellular materials: A review on their mechanical properties towards fatigue-tolerant design and fabrication". In: *Materials Science and Engineering: R: Reports* 144 (2021), p. 100606. ISSN: 0927-796X. DOI: https://doi.org/10.1016/j.mser.2021.100606. URL: https://www.sciencedirect.com/science/article/pii/S0927796X21000012.

[4] Correlated Solutions. *VIC-2D v6 Full-Field Deformation Measurement System*. URL: https://www.correlatedsolutions.com/wp-content/uploads/2013/10/VIC-2D-Datasheet.pdf.

[5] T. DebRoy, H.L. Wei, J.S. Zuback, T. Mukherjee, J.W. Elmer, J.O. Milewski, A.M. Beese, A. Wilson-Heid, A. De, and W. Zhang. "Additive manufacturing of metallic components – Process, structure and properties". In: *Progress in Materials Science* 92 (2018), pp. 112–224. ISSN: 0079-6425. DOI: https://doi.org/10.1016/j.pmatsci.2017.10.001. URL: https://www.sciencedirect.com/science/article/pii/S0079642517301172.

[6] V.S. Deshpande, M.F. Ashby, and N.A. Fleck. "Foam topology: bending versus stretching dominated architectures". In: *Acta Materialia* 49.6 (2001), pp. 1035–1040. ISSN: 1359-6454. DOI: https://doi.org/10.1016/S1359-6454(00)00379-7. URL: https://www.sciencedirect.com/science/article/pii/S1359645400003797.

[7] G.P. Dinda, A.K. Dasgupta, and J. Mazumder. "Laser aided direct metal deposition of Inconel 625 superalloy: Microstructural evolution and thermal stability". In: *Materials Science and Engineering: A* 509.1 (2009), pp. 98–104. ISSN: 0921-5093. DOI: https://doi.org/10.1016/j.msea.2009.01.009. URL: https://www.sciencedirect.com/science/article/pii/S0921509309000215.

[8] Norman E. Dowling. *Mechanical Behavior of Materials*. 4th ed. Harlow: Pearson, 2013.

[9] Anton du Plessis, Seyed Mohammad Javad Razavi, Matteo Benedetti, Simone Murchio, Martin Leary, Marcus Watson, Dhruv Bhate, and Filippo Berto. "Properties and applications of additively manufactured metallic cellular materials: A review". In: *Progress in Materials Science* 125 (2022), p. 100918. ISSN: 0079-6425. DOI: https://doi.org/10.1016/j.pmatsci.2021.100918. URL: https://www.sciencedirect.com/science/article/pii/S0079642521001420.

[10] Fatec engineering. *What is the Difference between Low High Cycle Fatigue?* URL: https://www.fatec-engineering.com/2018/08/23/what-is-the-difference-between-low-high-cycle-fatigue/.

[11] Ke-yun Feng, Peng Liu, Huai-xue Li, Si-yu Sun, Shu-bo Xu, and Jia-ning Li. "Microstructure and phase transformation on the surface of Inconel 718 alloys fabricated by SLM under 1050°C solid solution + double ageing". In: *Vacuum* 145 (2017), pp. 112–115. ISSN: 0042-207X. DOI: https://doi.org/10.1016/j.vacuum.2017.08.044. URL: https://www.sciencedirect.com/science/article/pii/S0042207X17310928.

[12] B. Gorny, T. Niendorf, J. Lackmann, M. Thoene, T. Troester, and H.J. Maier. "In situ characterization of the deformation and failure behavior of non-stochastic porous structures processed by selective laser melting". In: *Materials Science and Engineering: A* 528.27 (2011), pp. 7962–7967. ISSN: 0921-5093. DOI: https://doi.org/10.1016/j.msea.2011.07.026. URL: https://www.sciencedirect.com/science/article/pii/S0921509311008057.

[13] D D Gu, W Meiners, K Wissenbach, and R Poprawe. "Laser additive manufacturing of metallic components: materials, processes and mechanisms". In: *International Materials Reviews* 57.3 (2012), pp. 133–164. DOI: 10.1179/1743280411Y.0000000014. eprint: https://doi.org/10.1179/1743280411Y.0000000014. URL: https://doi.org/10.1179/1743280411Y.0000000014.

[14] Recep Gümrük, R.A.W. Mines, and Sami Karadeniz. "Static mechanical behaviours of stainless steel micro-lattice structures under different loading conditions". In: *Materials Science and Engineering: A* 586 (2013), pp. 392–406. ISSN: 0921-5093. DOI: https://doi.org/10.1016/j.msea.2013.07.070. URL: https://www.sciencedirect.com/science/article/pii/S092150931300840X.

[15] Lena Huynh, John Rotella, and Michael D. Sangid. "Fatigue behavior of IN718 microtrusses produced via additive manufacturing". In: *Materials Design* 105 (2016), pp. 278–289. ISSN: 0264-1275. DOI: https://doi.org/10.1016/j.matdes.2016.05.032. URL: https://www.sciencedirect.com/science/article/pii/S0264127516306335.

[16] Yasuhiro Kakinuma, Masahiko Mori, Yohei Oda, Takanori Mori, Makoto Kashihara, Adam Hansel, and Makoto Fujishima. "Influence of metal powder characteristics on product quality with directed energy deposition of Inconel 625". In: *CIRP Annals* 65.1 (2016), pp. 209–212. ISSN: 0007-8506. DOI: https://doi.org/10.1016/j.cirp.2016.04.058. URL: https://www.sciencedirect.com/science/article/pii/S0007850616300580.

[17] Ryo Koike, Taro Misawa, Tojiro Aoyama, and Masaki Kondo. "Controlling metal structure with remelting process in direct energy deposition of Inconel 625". In: *CIRP Annals* 67.1 (2018), pp. 237–240. ISSN: 0007-8506. DOI: https://doi.org/10.1016/j.cirp.2018.04.061. URL: https://www.sciencedirect.com/science/article/pii/S0007850618300854.

[18] Radomila Konečná, Gianni Nicoletto, Ludvík Kunz, and Adrián Bača. "Microstructure and directional fatigue behavior of Inconel 718 produced by selective laser melting". In: *Procedia Structural Integrity* 2 (2016). 21st European Conference on Fracture, ECF21, 20-24 June 2016, Catania, Italy, pp. 2381–2388. ISSN: 2452-3216. DOI: https://doi.org/10.1016/j.prostr.2016.06.298. URL: https://www.sciencedirect.com/science/article/pii/S2452321616303092.

[19] Martin Leary, Maciej Mazur, Joe Elambasseril, Matthew McMillan, Thomas Chirent, Yingying Sun, Ma Qian, Mark Easton, and Milan Brandt. "Selective laser melting (SLM) of AlSi12Mg lattice structures". In: *Materials Design* 98 (2016), pp. 344–357. ISSN: 0264-1275. DOI: https://doi.org/10.1016/j.matdes.2016.02.127. URL: https://www.sciencedirect.com/science/article/pii/S0264127516302726.

[20] Martin Leary et al. "Inconel 625 lattice structures manufactured by selective laser melting (SLM): Mechanical properties, deformation and failure modes". In: *Materials Design* 157 (2018), pp. 179–199. ISSN: 0264-1275. DOI: https://doi.org/10.1016/j.matdes.2018.06.010. URL: https://www.sciencedirect.com/science/article/pii/S0264127518304763.

[21] I. Maskery, N.T. Aboulkhair, A.O. Aremu, C.J. Tuck, and I.A. Ashcroft. "Compressive failure modes and energy absorption in additively manufactured double gyroid lattices". In: *Additive Manufacturing* 16 (2017), pp. 24–29. ISSN: 2214-8604. DOI: https://doi.org/10.1016/j.addma.2017.04.003. URL: https://www.sciencedirect.com/science/article/pii/S2214860417301203.

[22] I. Maskery, A.O. Aremu, L. Parry, R.D. Wildman, C.J. Tuck, and I.A. Ashcroft. "Effective design and simulation of surface-based lattice structures featuring volume fraction and cell type grading". In: *Materials Design* 155 (2018), pp. 220–232. ISSN: 0264-1275. DOI: https://doi.org/10.1016/j.matdes.2018.05.058. URL: https://www.sciencedirect.com/science/article/pii/S026412751830443X.

[23] S. McKown, Y. Shen, W.K. Brookes, C.J. Sutcliffe, W.J. Cantwell, G.S. Langdon, G.N. Nurick, and M.D. Theobald. "The quasi-static and blast loading response of lattice structures". In: *International Journal of Impact Engineering* 35.8 (2008). Twenty-fifth Anniversary Celebratory Issue Honouring Professor Norman Jones on his 70th Birthday, pp. 795–810. ISSN: 0734-743X. DOI: https://doi.org/10.1016/j.ijimpeng.2007.10.005. URL: https://www.sciencedirect.com/science/article/pii/S0734743X07001376.

[24] Amir Mostafaei, S. Harsha Vardhan R. Neelapu, Cameron Kisailus, Lauren M. Nath, Tevis D.B. Jacobs, and Markus Chmielus. "Characterizing surface finish and fatigue behavior in binder-jet 3D-printed nickel-based superalloy 625". In: *Additive Manufacturing* 24 (2018), pp. 200–209. ISSN: 2214-8604. DOI: https://doi.org/10.1016/j.addma.2018.09.012. URL: https://www.sciencedirect.com/science/article/pii/S2214860418304810.

[25] Jochen Mueller and Kristina Shea. "Buckling, build orientation, and scaling effects in 3D printed lattices". In: *Materials Today Communications* 17 (2018), pp. 69–75. ISSN: 2352-4928. DOI: https://doi.org/10.1016/j.mtcomm.2018.08.013. URL: https://www.sciencedirect.com/science/article/pii/S2352492818302733.

[26] Lawrence E. Murr, Sara M. Gaytan, Diana A. Ramirez, Edwin Martinez, Jennifer Hernandez, Krista N. Amato, Patrick W. Shindo, Francisco R. Medina, and Ryan B. Wicker. "Metal Fabrication by Additive Manufacturing Using Laser and Electron Beam Melting Technologies". In: *Journal of Materials Science Technology* 28.1 (2012), pp. 1–14. ISSN: 1005-0302. DOI: https://doi.org/10.1016/S1005-0302(12)60016-4. URL: https://www.sciencedirect.com/science/article/pii/S1005030212600164.

[27] J.P. Oliveira, A.D. LaLonde, and J. Ma. "Processing parameters in laser powder bed fusion metal additive manufacturing". In: *Materials Design* 193 (2020), p. 108762. ISSN: 0264-1275. DOI: https://doi.org/10.1016/j.matdes.2020.108762. URL: https://www.sciencedirect.com/science/article/pii/S0264127520302963.

[28] Olympus. *Microscope BX53M*. URL: https://www.olympus-ims.com/en/microscope/bx53m/.

[29] SLM Solutions. *AL Alloy - Alsi10Mg Material Data Sheet*. URL: https://www.slm-solutions.com/fileadmin/Content/Powder/MDS/MDS_Al-Alloy_AlSi10Mg_0520_EN.pdf.

[30] Bartłomiej Wysocki, Piotr Maj, Ryszard Sitek, Joseph Buhagiar, Krzysztof Jan Kurzydłowski, and Wojciech Świeszkowski. "Laser and Electron Beam Additive Manufacturing Methods of Fabricating Titanium Bone Implants". In: *Applied Sciences* 7.7 (2017). ISSN: 2076-3417. DOI: 10.3390/app7070657. URL: https://www.mdpi.com/2076-3417/7/7/657.

[31] Zefeng Xiao, Yongqiang Yang, Ran Xiao, Yuchao Bai, Changhui Song, and Di Wang. "Evaluation of topology-optimized lattice structures manufactured via selective laser melting". In: *Materials Design* 143 (2018), pp. 27–37. ISSN: 0264-1275. DOI: https://doi.org/10.1016/j.matdes.2018.01.023. URL: https://www.sciencedirect.com/science/article/pii/S0264127518300303.

[32] Chunze Yan, Liang Hao, Ahmed Hussein, Simon Lawrence Bubb, Philippe Young, and David Raymont. "Evaluation of light-weight AlSi10Mg periodic cellular lattice structures fabricated via direct metal laser sintering". In: *Journal of Materials Processing Technology* 214.4 (2014), pp. 856–864. ISSN: 0924-0136. DOI: https://doi.org/10.1016/j.jmatprotec.2013.12.004. URL: https://www.sciencedirect.com/science/article/pii/S0924013613003804.

[33] Chunze Yan, Liang Hao, Ahmed Hussein, and David Raymont. "Evaluations of cellular lattice structures manufactured using selective laser melting". In: *International Journal of Machine Tools and Manufacture* 62 (2012), pp. 32–38. ISSN: 0890-6955. DOI: https://doi.org/10.1016/j.ijmachtools.2012.06.002. URL: https://www.sciencedirect.com/science/article/pii/S0890695512001095.

[34] Chunze Yan, Liang Hao, Ahmed Hussein, Philippe Young, Juntong Huang, and Wei Zhu. "Microstructure and mechanical properties of aluminium alloy cellular lattice structures manufactured by direct metal laser sintering". In: *Materials Science and Engineering: A* 628 (2015), pp. 238–246. ISSN: 0921-5093. DOI: https://doi.org/10.1016/j.msea.2015.01.063. URL: https://www.sciencedirect.com/science/article/pii/S0921509315000908.

[35] Chunze Yan, Liang Hao, Ahmed Hussein, Philippe Young, and David Raymont. "Advanced lightweight 316L stainless steel cellular lattice structures fabricated via selective laser melting". In: *Materials Design* 55 (2014), pp. 533–541. ISSN: 0261-3069. DOI: https://doi.org/10.1016/j.matdes.2013.10.027. URL: https://www.sciencedirect.com/science/article/pii/S0261306913009540.

[36] S. Zhao, S.J. Li, W.T. Hou, Y.L. Hao, R. Yang, and R.D.K. Misra. "The influence of cell morphology on the compressive fatigue behavior of Ti-6Al-4V meshes fabricated by electron beam melting". In: *Journal of the Mechanical Behavior of Biomedical Materials* 59 (2016), pp. 251–264. ISSN: 1751-6161. DOI: https://doi.org/10.1016/j.jmbbm.2016.01.034. URL: https://www.sciencedirect.com/science/article/pii/S1751616116000382.

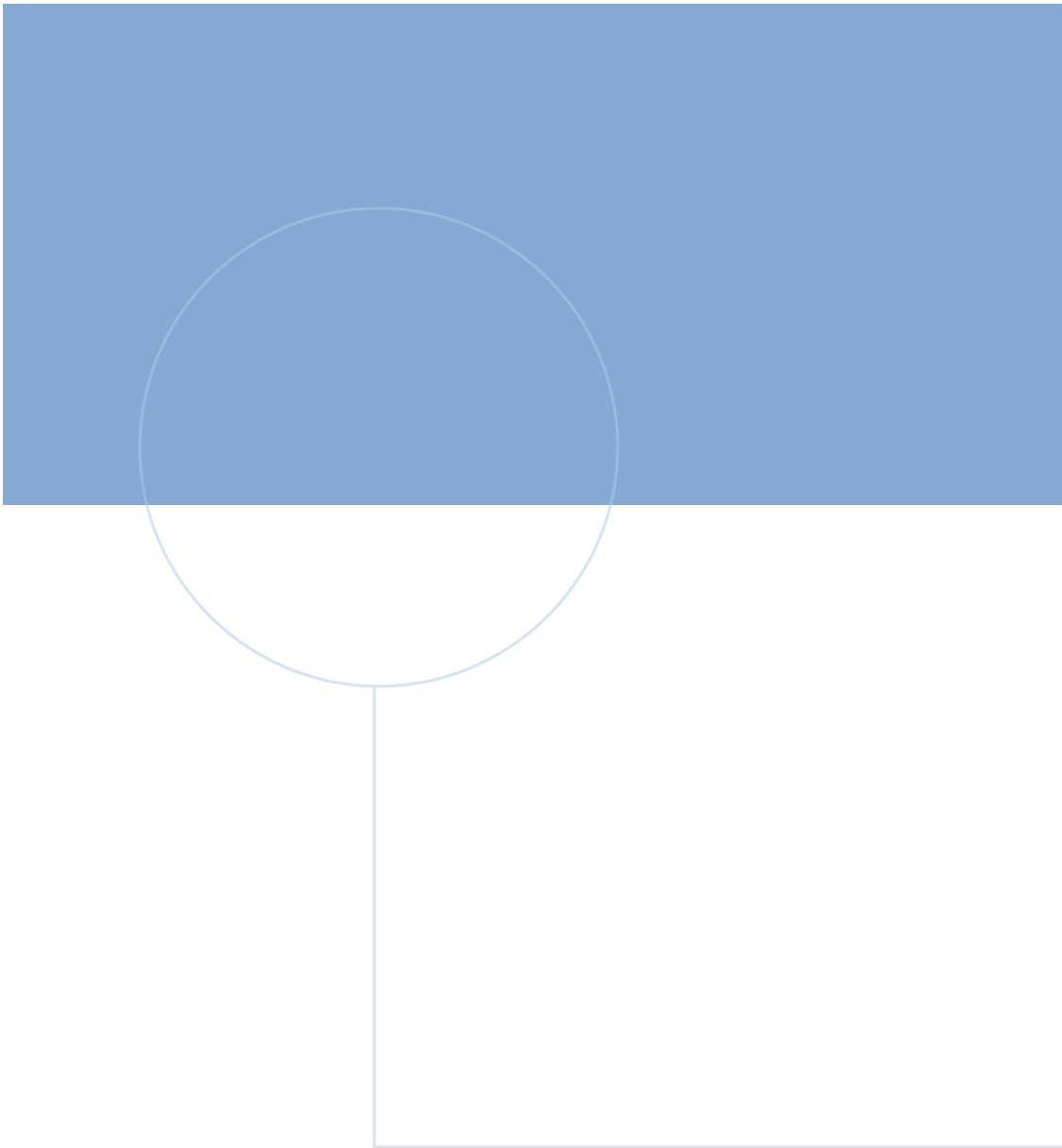

NTNU

Kunnskap for en bedre verden